Øyvind Nielsen

# Mushy zone permeability and grain morphology in equiaxed aluminium-copper alloys

NTNU Trondheim
Norges teknisk-naturvitenskapelige universitet

Doktor ingeniøravhandling 2000:33
Institutt for materialteknologi og elektrokjemi

IME-rapport 2000:14

# Mushy zone permeability and grain morphology in equiaxed aluminium-copper alloys

by

Øyvind Nielsen

March, 2000



The Norwegian University of Science and Technology

This thesis has been submitted to The Norwegian University of Science and Technology (NTNU) in partial fulfilment of the requirements for the degree 'Doktor Ingeniør'.

# Acknowledgements

The work presented in this thesis was carried out at the Department of Materials Technology and Electrochemistry of The Norwegian University of Science and Technology under the supervision of Professor Lars Arnberg and Professor Asbjørn Mo (The University of Oslo). The work was funded by the Brite-EuRam project EMPACT with Project No.BE-1112 and Contract No.BRPR-CT95-0112.[1] I thank the EMPACT Partners and the European Commission for financial support.

I want to express my gratitude to Professor Lars Arnberg for scientific advise and valuable discussions throughout the thesis work. His support and encouragement during periods of frustration and despair has been invaluable. Thanks are also due to Professor Asbjørn Mo for being an excellent teacher in the subject of scientific writing and for his patient guidance in the field of mathematical modelling. I am also very grateful to Dr. Håvard Thevik, who was responsible for the Norwegian part of the EMPACT Project during the main part of my thesis work, for his valuable suggestions and interest concerning the permeability measurements and for including me in the Norwegian as well as in the European EMPACT Project Teams.

In addition, I would like to thank the industrial participants in the Norwegian EMPACT Project Team consisting of Mr. Einar Jensen, Dr. Bjørn Rune Henriksen, Mr. Arild Håkonsen, and Dr. Steinar Benum. The encouraging support and creative suggestions from this forum were important in the work with the experimental methods.

The work with Article 3 was carried out in close collaboration with researchers at the Ecole Nationale Supérieure des Mines de Nancy in France through Dr. Benoît Appolaire's post doctoral position at SINTEF Oslo. Dr. Appolaire is greatly acknowledged for sharing his insight in equiaxed crystal growth and for his efforts in applying this insight to model the cumbersome case of inoculated aluminium alloys.

I also feel indebted to my closest fellow students Dr. Liss Pedersen and Mr. Thordur Magnusson for valuable discussions, encouragement, and friendship. Thanks are also due to Dr. Ivar Farup and Dr. Mohammed M'Hamdi for always having time for scientific discussions and valuable suggestions during my stay at SINTEF Oslo.

[1]The EMPACT Project consisted of the following participants: Hoogovens Corporate Services BV (The Netherlands); Hydro Aluminium AS (Norway); Elkem Aluminium ANS (Norway); Pechiney Recherche (France); Vereinigte Aluminiumwerke AG (Germany); Alusuisse-Lonza Services AG (Switzerland); Calcom SA (Switzerland); Technische Universiteit Delft (The Netherlands); Institut National Polytechnique de Lorraine (France); Ecole Polytechnique Federale de Lausanne (Switzerland); Institutt for Energiteknikk (Norway); and SINTEF (Norway).

When it comes to the experimental part of the work, thanks are due to Mr. Wilhelm Dall for help on the solidification laboratory and to Ms. Tone Anzjøn, Ms. Birgitte Karlsen, Ms. Gisela Berg, and Ms. Irene Furulund for help with the sample preparation and optical microscopy. Ms. Anne Lise Dons and Mr. Per Kolby are acknowledged for providing me with phase diagrams from ThermoCalc and thermophysical data. Mr. Brian Cochran at Wabash Alloys LLC, Indiana, USA, is acknowledged for providing me very rapidly with chemical analyses of the Al-Cu alloys. Dr. Dag Mortensen and Dr. Hallstein Hemmer at Institutt for Energiteknikk (Kjeller, Norway), are acknowledged for suggesting and performing the electron-beam welding, which lead to a break-through in the work with the permeameter.

Finally, I would to thank my family for their encouragement and support over the years, and my wife, Hilde Dorthea, for all her support and for sharing my frustrations as well as, on rare occasions, the feeling of success.

Oslo, March 2000

Øyvind Nielsen

# Contents

# Summary

This thesis has addressed the assessment of the mushy zone permeability in equiaxed aluminium alloys. The approach taken has been to experimentally determine the permeability of binary Al-Cu alloys as a function of a set of parameters describing the microstructural morphology. Moreover, the morphology parameters have been experimentally determined during solidification of binary Al-Cu alloys in order to evaluate the morphology predicted by an equiaxed growth model commonly used in micro-macro modelling. The thesis is presented as three free-standing articles.

In Article 1, a new experimental apparatus for measuring the mushy zone permeability of aluminium alloys has been presented. The apparatus is capable of detecting differences in permeability resulting from very small differences in microstructural morphology. Permeabilities have been measured for high solid fractions (0.68 to 0.91) and different grain morphologies. Characterisation of the microstructural morphology on both the intragranular and extragranular length scales have been performed on the samples. The results are in fairly good agreement with the predictions of the Kozeny-Carman relation and with more recent theory that takes flow partitioning between intragranular and extragranular regions into account. The validation of these permeability models is an important progress because models that predict the formation of casting defects are often very sensitive to the permeability.

In Article 2, general principles and experimental difficulties associated with the measurement of permeability in aluminium alloys have been discussed in order to ease a further development of experimental methods suitable for such measurements. In order to avoid the surface tension effects associated with liquid/gas interfaces in the narrow channels of the mushy zone, a flux melt can be used at the inlet of the permeameter. Electron-beam welding has been shown to be a suitable method for ensuring a complete wetting between sample and flux after remelting to the test temperature. Moreover, the influence of the permeameter design and the experimental procedure on grain detachment, preferred flow channel formation, and coarsening have been revealed through microstructure images.

In Article 3, the morphology predicted by an equiaxed growth model recently presented elsewhere has been compared with quantitative experimental morphology measurements on a range of Al-Cu alloys. In the experiments, the samples have been solidified with uniform temperature and quenched from the mushy state at the instant when the eutectic temperature was reached. The copper content and the amount of grain refiner additions have been varied, resulting in both 'clover-leaf' and dendritic equiaxed morphologies. Morphology characterisation on both the intragranular and extragranular length scales has been performed on the quenched samples. Average heat extraction rates, grain

densities, and alloy compositions from the experiments have been used as input to the equiaxed grain growth model, and the resulting morphology predictions have been compared with the morphology measurements. For the morphologies observed in the present study, the equiaxed growth model predicts higher values of the internal solid fraction than observed experimentally. This has been indicated to be due to the failure of commonly made modelling assumptions during the later stages of the solidification.

Because we lack a validated model for the development of the parameters at which the permeability depend, we can not expect to have a very accurate prediction of the permeability during solidification. The results from the experiments in this thesis indicate that the accuracy of the permeability used in solidification models is, presently, limited by the assumptions concerning the morphology development rather than by the assumptions concerning the relation between the morphology and the permeability.

# Introduction

The objectives of this thesis work are to experimentally investigate (*i*) the relation between the mushy zone permeability and the grain morphology, and (*ii*) the development of the grain morphology during equiaxed solidification of aluminium alloys. The motivation for the work will be presented in this introduction along with an outline of the thesis.

## 1 Industrial motivation

Aluminium metal is produced either by electrolysis of alumina or by remelting of secondary aluminium. Both of these processes produce liquid metal that must in turn be solidified in a casting process. In continuous and semi-continuous casting (DC casting, strip casting, wire casting, etc.) and in shape casting, defects like macrosegregation, porosity, and hot tears are often present. Macrosegregation denotes inhomogeneous distribution of alloying elements at the scale of the casting. Such defects can require costly treatments of the cast products prior to further processing (e.g., surface scalping of ingots prior to rolling) and can have a fatal influence on the properties in the final products (e.g., rejection of a shaped casting due to hot tearing). Due to the large production volumes involved in these casting processes, small reductions in the amount of defects can give a large economical profit. Such improvements can in many cases be difficult to achieve without a better understanding of the physical phenomena that control the processes.

The main industrial motivation for the present study is the need for a better understanding and quantitative predictions of macrosegregation formation during DC casting of wrought aluminium alloys. A schematic view of the DC casting process is given in Figure 1 along with a typical macrosegregation pattern. The physical mechanisms responsible for macrosegregation formation in general with examples from DC casting of aluminium alloys are discussed subsequently.

## 2 Mechanisms for macrosegregation in DC casting

Due to the extensive use of inoculants in DC casting of wrought aluminium alloys and the efficient grain refining effect of such additions, solidification generally occurs by the formation of equiaxed grains. Equiaxed solidification of alloys can be illustrated by the schematic binary phase diagram in Figure 2. A melt with a nominal composition $w_0$ that is cooled to a temperature $T^*$ in the mushy zone (i.e., between the liquidus, $T_{liq}$, and the

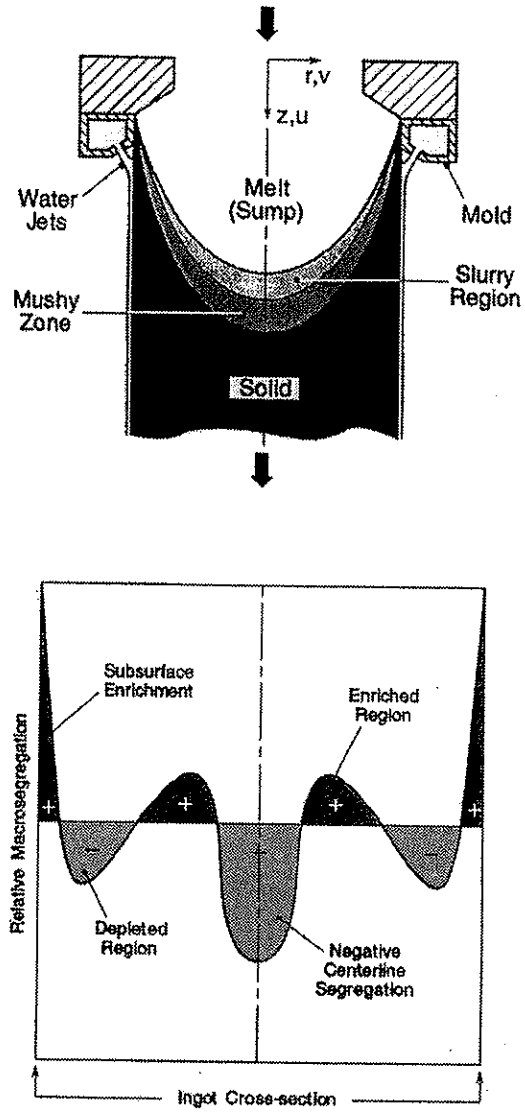


Figure 1: *The DC casting process and commonly observed macrosegregation concentration profile in a cross-section of the cast ingot. From Reference [1].*

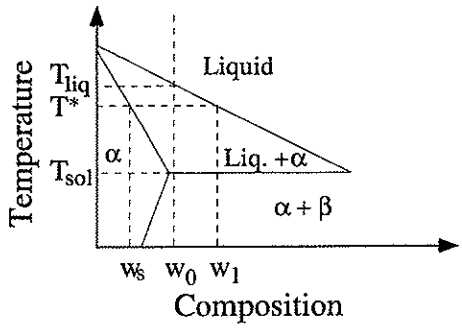


Figure 2: *Schematic sketch of a binary phase diagram. The symbols are explained in the text.*

solidus, $T_{sol}$) will experience a driving force for solidification. The thermodynamically stable situation at $T^*$ is a mixture of solid with composition $w_s$ and liquid with composition $w_l$ in fractions given by the solute conservation. For a given undercooling, $T_{liq} - T^*$, a number of nuclei will become active and grains with composition $w_s$ will start to grow from the liquid. The rate of solidification is controlled by the heat extraction rate and the rate of solute removal from the solid/liquid interface by diffusion in the solid and by diffusion and convection in the liquid.

During equiaxed solidification, two different regimes can be distinguished: (*i*) the free crystal regime where the grains are small compared with their final sizes and free to move in the liquid; and (*ii*) the packed bed regime, where the grains have impinged on each other so that the movement of a grain is limited by the movement of the neighbouring grains (Figure 3). The transition between the two regimes is commonly referred to as dendrite coherency [2,3].

In both regimes, macrosegregation can result from flow of liquid due to a spatial variation in the liquid density, i.e., thermo-solutal convection. The density differences cause a flow of liquid between regions of the mushy zone having different temperatures and/or solute concentrations. In the free crystal regime, macrosegregation can result from the transport of grains in the liquid due to (*i*) density differences between the liquid and the solid phases, and (*ii*) the flow fields set up by natural or forced convection in the liquid. For example, transport of equiaxed grains poor in solute can cause a region of negative segregation at the centreline of a DC cast ingot [5]. In the packed bed regime, macrosegregation can result from the flow of liquid in the coherent solid network due to solidification shrinkage or forced convection. For example, in DC casting of aluminium alloys, solidification shrinkage can cause a region of positive segregation close to the cast surface (inverse segregation). In addition, the pressure exerted on the mushy zone by the metallostatic head can cause forced convection and exudation of highly enriched liquid through the cast surface in the air-gap between the casting and the mould [6,7].

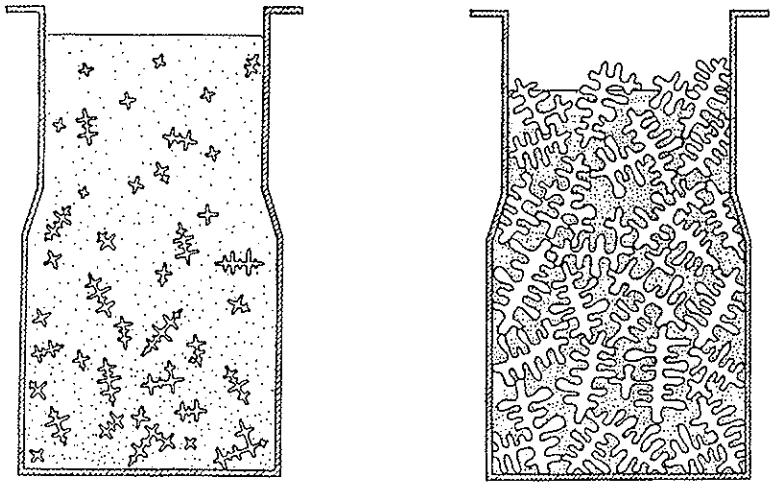

(a) The free crystal regime where the grains are small compared with their final sizes and free to move in the liquid

(b) The packed bed regime, where the grains have impinged on each other so that the movement of a grain is limited by the movement of the neighbouring grains

Figure 3: *The two different regimes observed during equiaxed solidification. From Reference [4].*

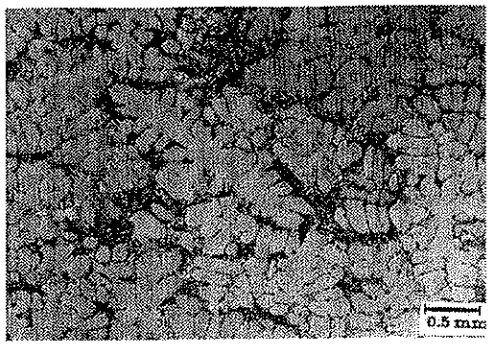


Figure 4: *The as-cast morphology of the primary aluminium phase of aluminium alloy A356. The dendritic morphology reveals the complex shape of the solid/liquid interface in a typical casting process that complicates the specification of the boundary conditions in microscopic solidification models. From Reference [8].*

In order to systematise the knowledge and to study the effect of different physical mechanisms on the macrosegregation formation, it is necessary to describe the casting process by a mathematical model. As will be explained subsequently, the mushy zone permeability and parameters describing the grain morphology are important quantities in the mathematical description of the formation of macrosegregation and casting defects in general.

# 3 Modelling of casting processes

## 3.1 Volume averaging

The microscopic balance equations for conservation of mass, momentum, energy, and solute must be fulfilled at each point within a casting. In principle, these equations could be solved within each phase present, which would give the velocity, the pressure, the stress, the temperature, and the solute content of each phase as a function of space and time. In reality, however, the complex shape of the phase interfaces present in most solidification processes complicates the specification of the boundary conditions and the front tracking in the mathematical problem (Figure 4).

In order to circumvent this problem, the microscopic conservation equations are commonly averaged over a macroscopic volume of the order of ($10^{-2}$–$10^{-3}$) m, resulting in a set of equations for each of the different phases present in the averaging volume [9]. The temperature is commonly assumed to be homogeneously distributed within the averaging volume, which is a good approximation for most casting processes involving aluminium alloys because of the high thermal diffusivity of aluminium [9].

## 3.2 Modelling of macrosegregation formation

In order to predict the macrosegregation formation during casting, the volume averaged equations for conservation of momentum in the liquid and solid phases must be solved. In the packed bed regime, which is the regime considered in this thesis, the solid velocity is constant and the momentum equation in the solid phase vanishes. The volume averaged equation for conservation of momentum in the liquid phase can be written [10][1]:

$$\frac{\partial}{\partial t}(\rho_l g_l \vec{v}_l) + \nabla \cdot (\rho_l g_l \vec{v}_l \vec{v}_l) = -g_l \nabla p_l + \mu_l \nabla \cdot (g_l \nabla \vec{v}_l) + g_l \rho_l \vec{g} - \vec{M}_l \tag{1}$$

where $\vec{v}_l$, $p_l$, and $g_l$ are the local volume averaged liquid velocity, the local liquid pressure and the volume fraction of liquid, respectively, and $t$ is the time. The quantities $\rho_l$, $\mu_l$, and $\vec{g}$ are the liquid density, the liquid viscosity, and the acceleration due to gravity, respectively. The left hand side of Eq. (1) represents the rate of change of the momentum of the liquid phase contained in a volume element. On the right hand side, the first term is the momentum change due to the local pressure gradient and the buoyancy forces; the second term is the momentum change due to the viscous stresses; and the third term is the momentum change due to the body forces (gravity). Finally, the fourth term, $\vec{M}_l$, is the solid/liquid interfacial drag caused by the stress interaction at the solid/liquid interface. This term represents the momentum transfer across the solid/liquid interface and can be expressed as:

$$\vec{M}_l = \frac{1}{V_0} \int_{A_s} \tau_l \cdot \vec{n}_l \, dA \tag{2}$$

where $V_0$ is the averaging volume, $A_s$ is the solid/liquid interfacial area, $\vec{n}_l$ is the unit vector of the solid/liquid interface, and $\tau_l$ is the deviatoric part of Cauchy's stress tensor (the shear stress). Thus, $\vec{M}_l$ is the tangential or friction force exerted on the liquid at the solid/liquid interface.

Because the information about the interfacial geometry of the phases is lost in the volume averaging process, the interfacial fluxes such as the solid/liquid interfacial drag must be described by constitutive models. As will be revealed subsequently, the solid/-liquid interfacial drag in the packed bed regime can be modelled by introducing the mushy zone permeability.

## 3.3 Modelling of the solid/liquid interfacial drag

In the packed bed regime, the solid/liquid interfacial drag causes a resistance to liquid flow in the coherent solid network. By applying a porous medium approach, the drag can

[1] It should be noted that the momentum change due to phase change as well as the dispersive fluxes of momentum are neglected in Eq. (1).

be modelled by Darcy's law:

$$\vec{M}_l = \frac{\mu_l \vec{V}}{K} \tag{3}$$

where $K$ is the mushy zone permeability and $\vec{V}$ is the superficial velocity defined by

$$\vec{V} = g_l(\vec{v}_l - \vec{v}_s) \tag{4}$$

The term $\vec{v}_s$ is the local volume averaged solid velocity, which is a constant in the packed bed regime.

Intuitively, the resistance to liquid flow in a solid network would depend at least on the solid fraction and on the grain morphology. For example, a dendritic grain morphology with a large interfacial area would give a larger resistance than a globular grain morphology with compact grains. As shown in Eq. (3), because the liquid viscosity is commonly assumed to be a constant, the effect of the morphology must be accounted for by the permeability. The permeability has often been expressed by the Kozeny-Carman relation [11]:

$$K = \frac{(1 - g_s)^3}{5S_s^2} \tag{5}$$

where $g_s$ is the volume fraction of solid and $S_s$ is the solid/liquid interfacial area concentration (solid/liquid interfacial area per unit volume). As pointed out by Wang *et al.* [12], the Kozeny-Carman relation is based on a single interfacial length scale, $S_s^{-1}$, which is of the same order of magnitude as the secondary dendrite arm spacing [13]. In reality, there are at least two length scales associated with equiaxed solidification: the secondary dendrite arm spacing and the grain size. In order to separate the effect of these two length scales on the permeability, the concept of a grain envelope can been introduced: the grain envelope is defined as a smooth surface connecting the outermost points of the grain such that its area is minimised [14] (Figure 5). The envelope sub-divides the liquid phase into an intragranular liquid phase (inside the envelope) and an extragranular liquid phase (outside the envelope). With this concept, three additional parameters that affect the permeability can be defined: the volume fraction of grain envelopes, $g_e$, the envelope/liquid interfacial area concentration, $S_e$, and the envelope form factor, $\phi_e$, which is defined as the surface area of a sphere with the same volume as the envelope divided by the actual surface area of the envelope [12]. As revealed in Figure 5, the parameters $g_s$ and $S_s$ characterise the morphology of the solid while the parameters $g_e$ and $S_e$ characterise the morphology of the envelope. In the general situation, the permeability would depend on all five parameters ($g_s$, $S_s$, $g_e$, $S_e$, and $\phi_e$), as revealed in Figure 5. Moreover, in the limiting case of a completely dendritic morphology ($g_e = 1$ and $S_e = 0$), the permeability would depend only on $g_s$ and $S_s$; and in the limiting case of a completely globular morphology ($g_s = g_e$ and $S_s = S_e$), the permeability would depend only on

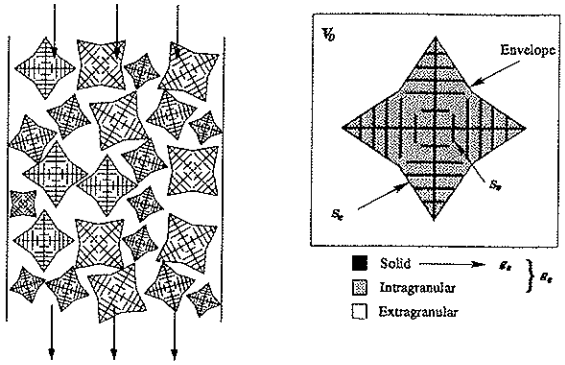


Figure 5: *Left: Fluid flow in a mushy zone composed of equiaxed grains. The resistance to flow depends both on the morphology of the intragranular zone (inside the envelope) and on the morphology of the extragranular zone (outside the envelopes). Right: The concept of a grain envelope and the definition of the intragranular and extragranular liquid phases.*

$g_e$ and $S_e$. Recently, Wang *et al.* [10] suggested an analytical model for the correlation between the permeability and the five morphology parameters mentioned previously. As opposed to the Kozeny-Carman relation, this model suggested by Wang *et al.* [10] has been developed to be valid in both the free crystal and packed bed regime.

In order to implement a constitutive relation between the permeability and parameters describing the grain morphology in a macrosegregation model, some assumptions must be made concerning the development of the grain morphology. In purely macroscopic macrosegregation calculations, where the solidification path is prescribed or calculated by assuming a complete mixing of solute in the liquid phase, the specific surface area $S_V = S_e/g_s$ is commonly assumed to be a constant. Thus, the Kozeny-Carman relation can be applied by expressing the permeability as a function of the solid fraction alone:

$$K(g_s) = K_0 \frac{(1-g_s)^3}{g_s^2} \quad \text{where} \quad K_0 = \frac{1}{5S_V^2} \tag{6}$$

The constant $K_0$ can be estimated from the as-cast secondary dendrite arm spacing by assuming a plate-like or cylindrical shape of the secondary dendrite arms. Alternatively, $K_0$ can be determined by fitting the calculated macrosegregation to macrosegregation measurements for a given case.

In micro-macro modelling of macrosegregation, the development of the parameters describing the grain morphology is commonly estimated by models that describe the solidification as a result of micro-scale phenomena [14–18]. Thus, the Kozeny-Carman relation in the form given by Eq. (5) or the permeability model suggested by Wang *et al.* [10] can be used to calculate the permeability from the predicted morphology.

# 4 Objectives and survey of the articles

As explained in Section 3.3, different relations between the mushy zone permeability and the grain morphology have been suggested in the literature. Due to a lack of reliable measurements of the permeability for aluminium alloys these relations have not been validated. Moreover, there is a lack of measurements of the development of the grain morphology parameters during equiaxed solidification of aluminium alloys. Thus, two unknown errors are induced in the permeability used in macrosegregation calculations: (*i*) the error in the permeability relation itself, and (*ii*) the error in the predicted morphology parameters, which indirectly gives a shift in the calculated permeability. The purpose of this thesis work is to shed light over this uncertainty in the permeability predictions by experimental investigations of (*i*) the relation between the mushy zone permeability and the grain morphology, and (*ii*) the development of the grain morphology during equiaxed solidification of aluminium alloys.

The articles included in the present work are:

**Article 1:** 'Experimental determination of mushy zone permeability in aluminium-copper alloys with equiaxed microstructures', by Ø. Nielsen, L. Arnberg, A. Mo, and H. Thevik. *Metallurgical and Materials Transactions A*, Vol. 30A, pp. 2455-62, 1999.

**Article 2:** 'Experimental difficulties associated with permeability measurements in aluminium alloys', by Ø. Nielsen and L. Arnberg. Submitted to the *Metallurgical and Materials Transactions*, March, 2000.

**Article 3:** 'Measurements and modelling of the microstructural morphology during equiaxed solidification of Al-Cu alloys', by Ø. Nielsen, B. Appolaire, H. Combeau, and A. Mo. Submitted to the *Metallurgical and Materials Transactions*, January, 2000.

The objective of the work presented in Article 1 is to develop a new experimental method for permeability measurements in aluminium alloys and to perform measurements at high solid fractions, where very few other measurements exist. The purpose is to compare the measurements with permeability models in the literature in order to evaluate the validity of using these models in macrosegregation modelling. A literature study of previous permeability measurements is given. The new permeameter and experimental method are described, and permeability measurements on equiaxed Al-Cu alloys with different grain morphologies are presented. A new metallographic technique for the separation of length scales in equiaxed microstructures is also presented along with quantitative morphology characterisation on the intragranular and extragranular length scale of the samples. Thus, the measurements can be compared with the predictions of the permeability model suggested by Wang *et al.* [10] as well as with the Kozeny-Carman

relation. This work has also been presented at the Third International Conference on Solidification and Gravity in Hungary, 1999 [19].

The objective of Article 2 is to reveal and discuss experimental difficulties associated with permeability measurements in aluminium alloys. There is still a need for permeability measurements for a large range of alloys and morphologies. However, in order to obtain permeability measurements that can be compared with relations between the permeability and the grain morphology, the experimental concept and permeameter design must be carefully chosen. General experimental principles are discussed, and a more thorough description of some of the experimental difficulties and solutions associated with the development of the permeameter in Article 1 is given.

The objective of Article 3 is to measure the grain morphology parameters at which the permeability depends at certain instants during equiaxed solidification of aluminium alloys. The purpose is to compare the measurements with morphology predictions obtained with an equiaxed growth model commonly used in micro-macro modelling, in order to evaluate the accuracy of the predictions and the corresponding error induced in the permeability predictions. The problems associated with quenching experiments for the purpose of assessing the grain morphology during growth of the primary aluminium phase is discussed. The grain morphology of Al-Cu alloys is revealed by quenching of the solidifying sample at the instant when the sample reaches the eutectic temperature. The metallographic method presented in Article 1 is further developed. The measured morphologies are compared with the predictions of the equiaxed growth model developed by B. Appolaire at INPL, France [14].

# References


[1] C. J. Vreeman, M. J. M. Crane, and F. P. Incropera. The effect of free-floating dendrites and convection on macrosegregation in direct chill cast aluminum alloys. Part I: model development. *International Journal of Heat and Mass Transfer*, **43**:677–686, 2000.

[2] R. J. Claxton. Aluminum alloy coherency. *Journal of Metals*, pages 14–16, February 1975.

[3] L. Arnberg, G. Chai, and L. Bäckerud. Determination of dendritic coherency in solidifying melts by rheological measurements. *Materials Science and Engineering*, **A173**:101–103, 1993.

[4] M. C. Flemings. Behavior of metal alloys in the semisolid state. *Metallurgical Transactions A*, **22A**:957–981, 1991.

[5] H. Yu and D. A. Granger. Macrosegregation in aluminum alloy ingot cast by the semicontinuous direct chill (DC) method. In *Aluminum Alloys: Their Physical and Mechanical Properties*, pages 17–29. EMAS, UK, 1986.

[6] M. C. Flemings. *Solidification processing*, chapter 7. McGraw-Hill, Inc., 1974.

[7] H. J. Thevik, A. Mo, and T. Rusten. A mathematical model for surface segregation in aluminium DC casting. *Metallurgical and Materials Transactions B*, **30B**:135–142, 1999.

[8] L. Arnberg, L. Bäckerud, and G. Chai. *Solidification characteristics of aluminum alloys*, volume 3: Dendritic coherency. AFS, Inc., 1996.

[9] J. Ni and C. Beckermann. A volume-averaged two-phase model for transport phenomena during solidification. *Metallurgical Transactions B*, **22B**:349–361, 1991.

[10] C. Y. Wang and C. Beckermann. Equiaxed dendritic solidification with convection: Part I. Multiscale/multiphase modeling. *Metallurgical and Materials Transactions A*, **27A**:2754–2764, 1996.

[11] P. C. Carman. *Flow of gases through porous media*, pages 11–13. Butterworth Scientific, London, 1956.

[12] C. Y. Wang, S. Ahuja, C. Beckermann, and H. C. de Groh III. Multiparticle interfacial drag in equiaxed solidification. *Metallurgical and Materials Transactions B*, **26B**:111–119, 1995.

[13] C. Y. Wang and C. Beckermann. A multiphase solute diffusion model for dendritic alloy solidification. *Metallurgical Transactions A*, **24A**:2787–2802, 1993.

[14] B. Appolaire. *Prise en compte du mouvement des cristaux équiaxes dans la modélisation de la solidification des lingots d'acier coules en fonderie.* PhD thesis, Institut National Polytechnique de Lorraine, France, 1999.

[15] M. Rappaz and Ph. Thévoz. Solute diffusion model for equiaxed dendritic growth. *Acta Metallurgica*, **35**:1487–1497, 1987.

[16] M. Rappaz and Ph. Thévoz. Solute diffusion model for equiaxed dendritic growth: Analytical solution. *Acta Metallurgica*, **35**:2929–2933, 1987.

[17] C. Y. Wang and C. Beckermann. A unified solute diffusion model for columnar and equiaxed dendrite alloy solidification. *Material Science and Engineering*, **A171**:199–211, 1993.

[18] C. Y. Wang and C. Beckermann. A multiphase solute diffusion model for dendritic alloy solidification. *Metallurgical and Materials Transactions A*, **24A**:2787–2802, 1993.

[19] Ø. Nielsen, L. Arnberg, A. Mo, and H. Thevik. Determination of mushy zone permeability in equiaxed Al-Cu alloys. In *Solidification and Gravity 2000*, pages 38–43. Trans Tech Publications Ltd, Switzerland, 1999.

# Article 1:

# Experimental determination of mushy zone permeability in aluminium-copper alloys with equiaxed microstructures

Ø. Nielsen* Lars Arnberg* Asbjørn Mo† Håvard Thevik‡

**Abstract**

An experimental apparatus for measuring the mushy zone permeability of aluminium-copper alloys with equiaxed microstructures has been constructed. Permeabilities have been measured for high solid fractions (0.68 to 0.91) and different dendrite morphologies. Microstructure characterisation on both the interdendritic and extradendritic length scales have been performed on the samples. The results are in fairly good agreement with the predictions of the Kozeny-Carman relation and with more recent theory that takes flow partitioning between interdendritic and extradendritic regions into account.

*Department of Materials Technology and Electrochemistry, Norwegian University of Science and Technology, 7491 Trondheim, Norway

†SINTEF Materials Technology, P. O. Box 124, Blindern, 0314 Oslo, Norway

‡Det Norske Veritas, N-1322 Høvik, Norway

# 1 Introduction

Mathematical modelling of melt flow phenomena during solidification of alloys requires that the macroscopic equations for conservation of momentum accounts for the solid-liquid interfacial drag. Below the dendritic coherency temperature, i.e., when the solidified grains constitute a coherent network, this drag term can be modelled by introducing the mushy zone permeability. For equiaxed dendritic solidification, the permeability, $K$, has often been expressed by the Kozeny-Carman relation [1]:

$$K = \frac{(1 - g_s)^3}{5S_s^2} \tag{1}$$

where $g_s$ is the volume fraction of solid and $S_s$ is the solid-liquid interfacial area concentration (solid-liquid interfacial area per unit volume).

Piwonka and Flemings [2] measured the permeability of Al-4.5 wt pct Cu by forcing liquid lead or gaseous nitrogen through a solidifying sample contained in a U-shaped tube. However, displacing the residual liquid with a different metal or alloy can cause local constitutional remelting/solidification, which invalidates the assumption of a uniform solid fraction in the sample. An experimental setup in which the residual liquid is displaced by a gas was also applied by Paradies *et al.* [3]. The surface tension associated with the gas-liquid interface within the mushy zone, however, causes a significant pressure drop which was not taken into account in References 2 and 3.

These problems were not present in the experimental setup presented by Streat and Weinberg [4]. They remelted a cylindrical sample of a lead-tin alloy to a temperature just above the eutectic and added a metallostatic head of eutectic lead-tin alloy to one end of the sample. Thus, the liquid flowing into the mushy zone had the same composition as the residual liquid. This principle has been used in several more recent works [5–9], as well as in the present study.

Murakami and Okamoto [5] measured permeability on borneol-paraffin alloys with globular grains at low solid fractions (0.52 to 0.73). In addition to the solid fraction, they measured the solid-liquid interfacial area concentration and reported a fairly good agreement with the Kozeny-Carman relation. Poirier and Ganesan [6] measured permeability on dendritic Al-15.6 wt pct Cu alloys, which coarsened to dendritic-globular or globular microstructures during the experiment. They calculated a dimensionless permeability based on measurements of the specific surface area (solid-liquid interfacial area per unit volume of solid). Poirier and Ocansey [7] measured permeability on dendritic alloys at low solid fractions (0.51 to 0.69) by using Pb-Sn alloys with microstructures less subjected to coarsening. Ocansey *et al.* [8] performed one permeability measurement at a solid fraction of 0.917 using the procedure described in Reference 6. Viswanathan *et al.* [9] measured the variation of permeability with holding time at constant solid fractions (0.662, 0.678, and 0.871) for binary Al-Cu alloys. Separate coarsening experiments were performed to

correlate permeability with the solid-liquid interfacial area concentration, and the results compared favourably with the Kozeny-Carman relation.

The Kozeny-Carman relation, Eq. (1), is based on a single interfacial length scale, $S_s^{-1}$, which is of the same order of magnitude as the secondary dendrite arm spacing [10]. In reality, there are at least two length scales associated with equiaxed dendritic solidification: the secondary dendrite arm spacing and the grain size. Recently, Wang *et al.* [11] suggested a constitutive relation for the permeability that takes both these length scales into account. By introducing a partitioning between liquid flowing *through* the dendritic grains (interdendritic) and *between* the grains (extradendritic), they related the permeability to five parameters characterising the solid morphology. Experimental validation of this relation in the regime where the solid forms a coherent network, however, is limited [11]. No measurements of all the relevant morphology parameters have as yet been presented.

The purpose of the present paper is to present a series of permeability measurements at high solid fractions with corresponding solid morphology characterisation on both the interdendritic and extradendritic length scales. The results are compared with Eq. (1) and with the theoretical work presented by Wang *et al.* [11]. Furthermore, random and systematic errors associated with the experiment are discussed.

# 2 Experimental

## 2.1 Samples

Binary Al-Cu samples were prepared from pure aluminium (99.86 wt pct) and copper. As shown in Table 1, seven alloys with different compositions were made and cast either as cylindrical rods in a graphite mould (14-mm diameter) or as a block (7x7x15 $cm^3$). Different amounts of commercial Al-5 wt pct Ti-1 wt pct B rod master alloy were added to achieve a variety of microstructures. Parts of the castings were chosen and machined to cylindrical samples with lengths of 60 mm and diameters of 13 mm.

The flux alloy, Al-Cu of eutectic composition, was prepared, cast as cylindrical rods, and machined to flux cylinders with a length of 30 mm and a diameter of 13 mm. Each of the previously mentioned cylindrical samples was then joined to a flux cylinder by electron beam welding in order to facilitate a complete wetting between sample and flux. Finally, each joined cylinder was machined to a diameter of 9.95 mm and cut on each side of the weld to give a flux length $H_0$=15 mm and a sample or mushy zone length of 50 mm.

Table 1: *The as-cast mushy zone samples characterised by the chemical composition and approximate values for the grain size (d) and the secondary dendrite arm spacing ($\lambda_2$). The compositions were measured using spectroscopic chemical analysis.*

| Number | Wt pct Cu | Wt pct Ti | $d(\mu m)$ | $\lambda_2(\mu m)$ |
|---|---|---|---|---|
| 1 | 15.8 | 0.02 | 60 | 15 |
| 2 | 12.9 | 0.005 | 800 | 15 |
| 3 | 13.1 | 0.014 | 110 | 30 |
| 4 | 10.1 | 0.006 | 70 | 15 |
| 5 | 15.8 | 0.009 | 200 | 50 |
| 6 | 10.0 | 0.009 | 250 | 50 |
| 7 | 6.2 | 0.007 | 230 | 60 |

## 2.2 Permeameter

A schematic sketch of the experimental setup is shown in Figure 1. The permeameter is a graphite cell with outer dimensions of 3.5x2x9 $cm^3$. The flow channels are cylindrical with diameters of 10.0 mm for the two vertical channels and 5.0 mm for the horizontal one. As shown in Figure 1, the welded cylinder of sample and flux was placed in the cell with a thin layer of salt powder (KCl–44.5 wt pct LiCl) on top of the flux to prevent oxidation. The main driving force for the flow was an argon pressure supplied through a vertical tube sealed to the permeameter with a ceramic cement. The applied pressure was adjusted with a needle valve and measured continuously using a transducer with a range of 0 to 350 mbar.

The graphite float resting on top of the exuding melt was attached by a thin metal wire to a displacement transducer with a range of 0 to 20 mm. Thus, the height of the exudate could be measured continuously as a function of time. The temperature in the sample was monitored with 1-mm thermocouples through holes in the graphite cell. The signals from the measuring devices were recorded using a 16-bit PC data acquisition card giving resolutions better than the general noise experienced during a measurement.

## 2.3 Procedure

The permeameter assembly was heated in a cylindrical resistance furnace to 1°C to 3°C above the eutectic temperature of the Al-Cu system (548°C). At this temperature, the eutectic flux remelted completely and the sample remelted to a liquid fraction equal to the eutectic fraction. A constant argon pressure (20 to 80 mbar) was applied to the flux surface, causing a melt flow through the coherent mushy zone into the horizontal channel (Figure 1). When the horizontal channel was filled, the float was lifted by the exudate,

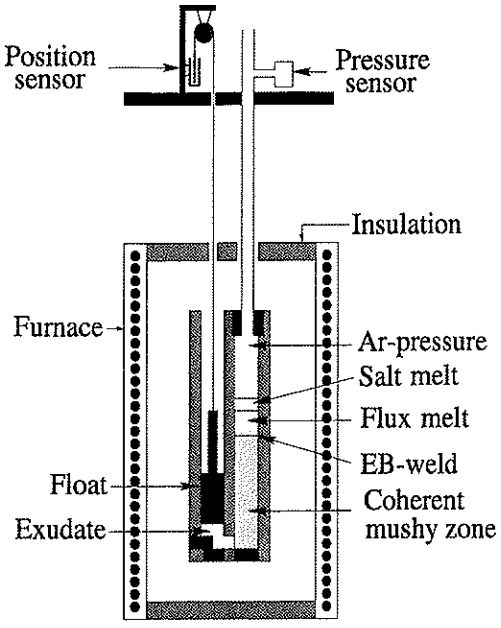


Figure 1: *Schematic sketch of the permeameter.*

and the level of the melt under the float was recorded as a function of time for about 50 seconds. The experiment was completed by releasing the pressure, lowering the furnace, and quenching the permeameter in water.

Because the moving liquid has near-eutectic composition, it should be noted that metallography on the quenched samples can easily distinguish between the phases that were solid and liquid during the experiment. Consequently, image analysis can provide an accurate description of the solid morphology during the experiment.

## 2.4 Metallography and image analysis

The quenched sample from each experiment was cut in various cross-sections, mechanically ground, and polished down to 1 $\mu$m. Etching in a 0.1 vol pct hydrogen fluoride solution for 1 minute produced a clear contrast between the primary Al phase and the Al-$Al_2Cu$ eutectic (Figure 2a). For each experiment, five representative gray-scale images were recorded from the samples. The images were analysed using automatic image analysis under the assumption that the eutectic corresponds to the liquid phase during the permeability measurement. The following morphological quantities were measured for each experiment: $g_s$, $S_s$, $g_e$, $S_e$, and $\phi_e$. These are defined subsequently. The quantities are reported as the mean value of the measurements on the five images with the cor-

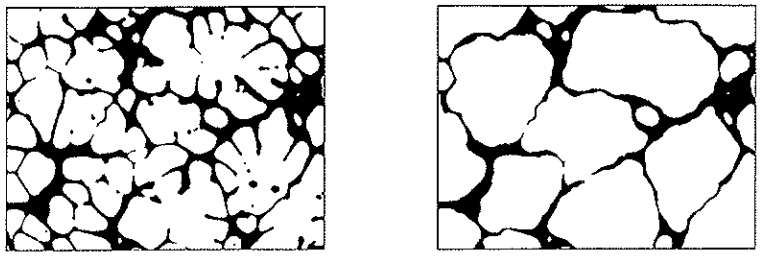

(a) (b)

Figure 2: *(a) Typical microstructure of quenched sample showing the white Al phase and the black* Al-$Al_2Cu$ *eutectic. Image used for estimation of* $g_s$ *and* $S_s$*. (b) Manual transformation of image (a), used for estimation of* $g_e$*,* $S_e$*, and* $\phi_e$*.*

responding standard error in the mean. Measurements from five images were considered sufficient, because increasing the number did not change the mean values significantly.

The volume fraction of solid in a sample, $g_s$, can be estimated by the area fraction of solid in an image, as shown by, e.g., Underwood [12] (Figure 2(a)). The interfacial area concentration, $S_s$, is defined as the area of the solid-liquid interface per unit volume [11]. This quantity should be distinguished from the specific surface area of solid, $S_V$, defined here as the area of the solid-liquid interface per unit volume of solid, and related to $S_s$ by

$$S_V = S_s/g_s \tag{2}$$

In stereology, $S_s$ is referred to as the surface-to-volume ratio [1] and can be estimated from an image by the formula [12]

$$S_s = (4/\pi)L_A \tag{3}$$

where $L_A$ is the perimeter of the solid-liquid interface per unit image area[2]. I should be noted that the perimeter measured by the automatic image analyser includes the part of the image frame intercepted by solid. This contribution equals the total frame perimeter multiplied by $g_s$ and must be subtracted from the measured perimeter in order to obtain $L_A$.

The grain envelope is defined as a smooth surface connecting the primary and secondary dendrite arms. In order to measure $g_e$, $S_e$, and $\phi_e$, the grain-envelopes were drawn manually, as shown in Figure 2(b). With this modified image, the volume fraction of

[1] In stereology and in References 5 and 9, the symbol $S_V$ is used to denote the area of the solid-liquid interface per unit volume, called $S_s$ in this study.

[2] The factor $(4/\pi)$ in Eq. (3) appears to be neglected by some authors [6, 13], while others do not describe the procedure used for measuring $S_s$ or $S_V$ [7, 9]

Table 2: *Values for acceleration due to gravity, viscosity, and density of flux melt.*

| Symbol | Value | Reference |
|---|---|---|
| $\mu_l$ | 0.0023kg/ms | [14] |
| $\rho_l$ | 3123kg/m$^3$ | [15] |
| $g$ | 9.82m/s$^2$ | – |

envelope, $g_e$, and the corresponding interfacial area concentration, $S_e$, were measured in the same way as $g_s$ and $S_s$ described previously.

The sphericity, $\phi_e$, of a grain-envelope is defined as the surface area of a sphere with the same volume as the envelope divided by the actual surface area of the envelope [11]. For a given grain-envelope in a two dimensional image, the sphericity was taken as the perimeter of a circle with area equal to the envelope area divided by the actual perimeter of the envelope. The sphericity in each image is then simply the average over three to five grain envelopes. This approach was considered to be sufficient because the permeability is much less sensitive to changes in the sphericity than to changes in the other morphological quantities [11]. In other words, only a crude estimate of $\phi_e$ is needed.

For each experiment, cross-sections of the quenched cylindrical samples were investigated for preferred flow channels. In cases where the applied pressure was high, these could sometimes be observed as small pools of eutectic. In addition, the exudate was investigated for grain fragments teared off by the forced convection. Experiments were discarded when one or both of these problems were observed.

# 3 Data analysis

As shown in Appendix A, the flow in the permeameter can be described as being one dimensional with a permeability given by

$$K = \frac{\mu_l V L_e}{\Delta P + \rho_l g L_v} \tag{4}$$

where $L_v$=47.5 mm and $L_e$=56.4 mm are the effective height and effective length of the mushy zone, respectively. The quantities $\mu_l$ and $\rho_l$ are the viscosity and density of the flux melt, respectively, and $g$ is the acceleration due to gravity, all given in Table 2. The term $V$ is the superficial velocity (volume fraction of liquid times the local volume averaged melt velocity), and $\Delta P$ is the pressure difference over the mushy zone. By taking into account the initial height of the flux melt on the pressurised side, $H_0$=15 mm, the average height of the exudate during the flow, $\bar{X}$, and the mass of the float system, $m_f$=2.9 g, the pressure difference can be written

$$\Delta P = P_{ext} + \rho_l g(H_0 - 2X_0 - 2\bar{X}) - m_f g/A \tag{5}$$

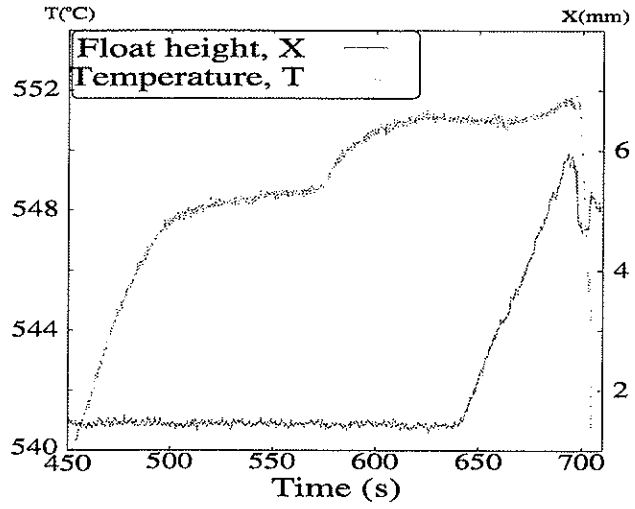


Figure 3: *Float height and temperature in a mushy zone sample as a function of time during a permeability measurement. Remelting of the eutectic starts at* $t \simeq 500$ s *and ends at* $t \simeq 575$ s. *Before quenching, the float movement can be represented by a straight line (*$t \simeq 640$ *to* 680 s*).*

where $P_{ext}$ is the applied gas pressure, $X_0$=5 mm is the initial height of the float, and $A$=78.5 mm$^2$ is the cross-sectional area of the float channel. Furthermore, mass conservation gives

$$V = \frac{dX(t)}{dt} \tag{6}$$

where $X(t)$ is the height of the float as a function of time, $t$. A plot of $X(t)$ from a typical experiment is shown in Figure 3 along with a plot of the temperature in the sample. It can be seen that in the time period (~50 seconds) during which the float moves, $X(t)$ is close to a straight line. According to Eq. (6), $V$ is then approximately a constant equal to the slope of a straight line fitted to $X(t)$. With the value of $V$ determined, the permeability for a given experiment can be calculated from Eqs. (4) and (5).

# 4 Results and error estimation

Table 3 gives the complete results from the permeability measurements, and Figure 4 shows representative examples of the quenched microstructures. No measurements were obtained for sample 4.

For samples 2, 3, and 5, repeated measurements were performed in order to estimate the random error in the permeability. However, due to slightly different coarsening of the

Table 3: *Results from the permeability measurements. The sample number is defined in Table 1.*

| Exp | Number | $g_s$ | $S_s[10^4\mathrm{m}^{-1}]$ | $g_e$ | $S_e[10^4\mathrm{m}^{-1}]$ | $\phi_e$ | $K[10^{-12}\mathrm{m}^2]$ |
|---|---|---|---|---|---|---|---|
| (a) | 1 | $\simeq g_e$ | $\simeq S_e$ | 0.680±0.006 | 8.04±0.08 | 0.90±0.01 | 1.11 |
| (b) | 2 | 0.786±0.005 | 5.38±0.05 | 0.969±0.003 | 0.9±0.09 | 0.69±0.04 | 0.36 |
| (c) | 2 | 0.769±0.002 | 5.72±0.05 | 0.957±0.003 | 1.3±0.1 | 0.75±0.04 | 0.52 |
| (d) | 3 | 0.738±0.005 | 4.72±0.07 | 0.837±0.005 | 2.6±0.1 | 0.82±0.02 | 1.9 |
| (e) | 3 | 0.743±0.004 | 4.26±0.03 | 0.841±0.004 | 2.39±0.07 | 0.83±0.01 | 2.16 |
| (f) | 5 | 0.753±0.007 | 3.1±0.1 | 0.833±0.006 | 1.9±0.1 | 0.84±0.01 | 3.4 |
| (g) | 5 | 0.73±0.01 | 3.2±0.1 | 0.82±0.01 | 1.9±0.1 | 0.84±0.01 | 4.2 |
| (h) | 6 | 0.829±0.009 | 2.9±0.1 | 0.907±0.006 | 1.51±0.07 | 0.67±0.04 | 0.92 |
| (i) | 7 | 0.910±0.007 | 2.1±0.1 | 0.961±0.005 | 0.97±0.09 | 0.80±0.04 | 0.36 |

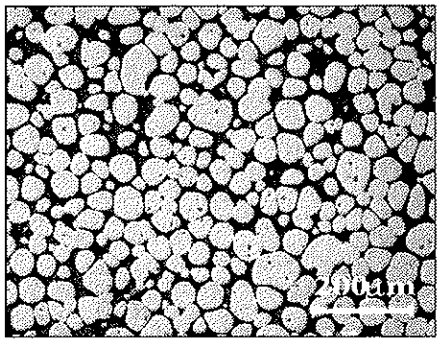

Experiment (a)

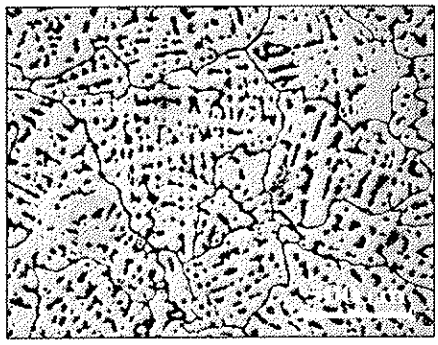

Experiment (b)

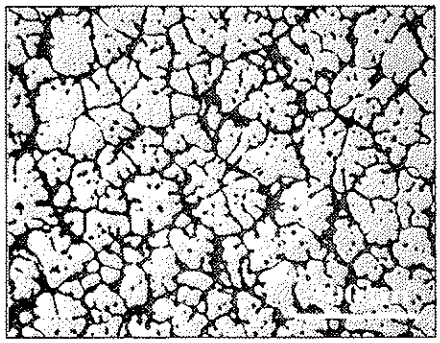

Experiment (d)

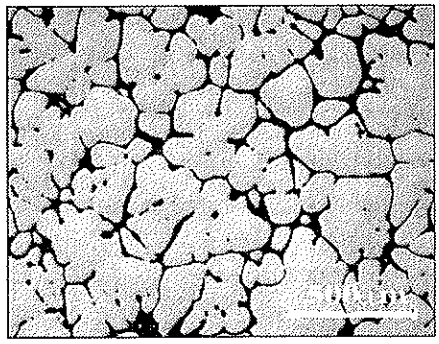

Experiment (h)

Figure 4: *Representative examples of quenched microstructures.*

initially identical samples, it turned out to be difficult to reproduce an experiment to the extent that the morphological quantities of the quenched samples were equal within errors. Such reproducibility was only achieved for two experiments on sample 3 in which the measured permeabilities were $2.10\times10^{-12}\mathrm{m}^2$ and $2.22\times10^{-12}\mathrm{m}^2$, respectively. These two values differ by 5 pct, which indicates that a permeability measurement is reproducible provided that the morphology of the sample can be reproduced. Averaging the morphological quantities and permeabilities for these two successfully repeated measurements gives result (e) in Table 3. The accuracy with which the permeability values are reported in Table 3 was chosen by *assuming* a relative error of 5 pct in each measurement.

The only measurable difference between the morphological quantities in experiments (f) and (g) is the 3 pct higher $g_s$ in (f), which is seen to result in a 20 pct lower permeability. This is reasonable and proves that the apparatus and procedure are capable of measuring the effect of very small morphology changes on the permeability.

For convenience, the test temperature was chosen to be 1°C to 3°C above the eutectic temperature, resulting in a liquid fraction somewhat above the eutectic fraction. However, because the liquid fraction, according to the lever rule, changes by approximately 0.003 per degree Celsius close to the eutectic point for the Al-Cu alloys used in this study, no correction was made for this effect.

# 5 Discussion

A common way of presenting permeability measurements is to plot a dimensionless permeability, $KS_V^2$, *vs* $g_s$. Figure 5 shows the results from Table 3 plotted in this form along with the Kozeny-Carman relation (Eq. (1)) and results from the literature.

As shown in Figure 5, most of the results from the present work are for high solid fractions, where very few other measurements exist. For the lower solid fractions, our results are of the same order of magnitude as previous results [5–9]. There is a large scatter in previous results. This has been suggested to be due to coarsening of the microstructure during the experiment, which makes it difficult to measure $S_V$ corresponding to the time at which $K$ is measured [8,9]. It was shown in Reference 14 that coarsening can have a significant influence on forced convection through a mushy zone. The analytical work by Wang *et al.* [11] indicates that the variables $g_s$ and $S_V$ alone cannot uniquely describe the permeability because they only represent one length scale: the dendrite arm spacing, $\lambda_2 \sim S_V^{-1}$ [10]. Consequently, two samples can have different permeabilities even for equal $g_s$ and $S_V$. This represents another possible explanation for the scatter in Figure 5.

A comparison between the measured data, the permeability relation suggested in Reference 11 (listed in Appendix B), and the Kozeny-Carman relation (Eq. (1)) is given in Figure 6. Using the measured morphological quantities in Table 3, the dimensionless permeabilities, $KS_V^2$, were calculated according to these two relations and plotted *vs* $g_s$

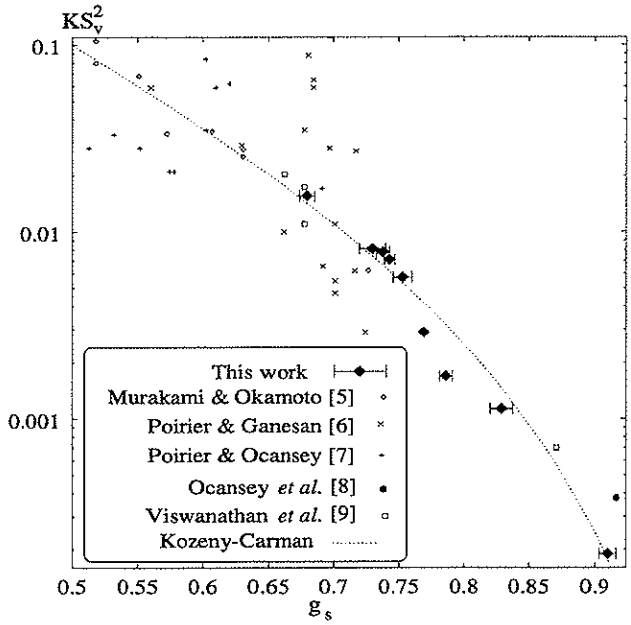


Figure 5: *Plot of the dimensionless permeability, $KS_V^2$, as a function of volume fraction of solid, $g_s$. Results of the present study are compared with other measurements and with the Kozeny-Carman relation.*

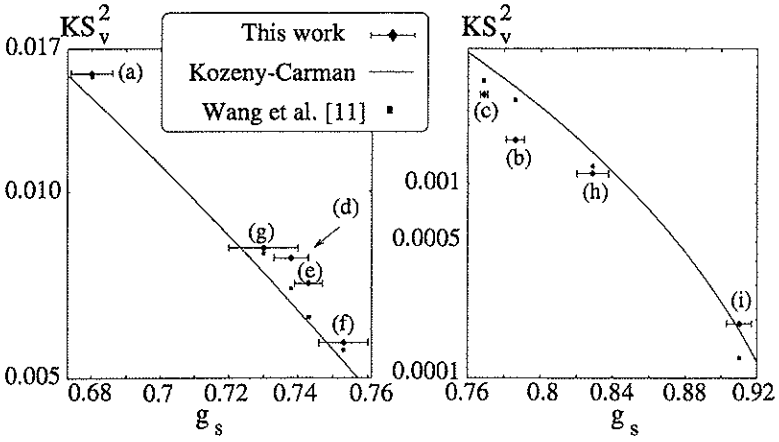


Figure 6: *Plot of the dimensionless permeability, $KS_V^2$, as a function of volume fraction of solid, $g_s$. Results of the present study are compared with Eq. (1) and the relation in Reference [11].*

along with the experimental results. It should be noted that the values calculated by the relation in Reference 11 can not be presented as a continuous curve because only one of the five independent variables are included in Figure 6. The flow partition coefficient, $\kappa_v$, defined as the ratio between the liquid flow rate passing *through* the dendritic grains (interdendritic) and the total flow rate through the system [11], can be calculated for each experiment using Eq. (B6), as shown in Table 4.

As shown in Figure 6(a), the permeability measured in experiment (a) is equal to the result predicted by the relation in Reference 11 and close to the Kozeny-Carman relation. Since the sample was completely globular in this experiment (Figure 4, experiment (a)), there was no interdendritic flow, and $\kappa_v$ equals zero. In this limiting case ($g_s$=$g_e$, $S_s$=$S_e$), the relation suggested by Wang *et al.* [11] reduces to a model presented by Happel [16], which deviates from the Kozeny-Carman relation with less than 15 pct for $g_s > 0.3$.

Experiments (b) and (c) are close to another limiting case, namely, $g_e$=1, where all the flow is through the interdendritic regions ($\kappa_v$ equals 89 and 94 pct for (b) and (c), respectively). It should be noted that the relation in Reference 11 reduces to the Kozeny-Carman relation in this limit. However, as can be observed in Figure 4, experiment (b), the microstructure has a very small but significant extradendritic liquid fraction, which constitutes channels between the grains. These are actually narrower than many of the interdendritic channels. Due to this, the permeabilities predicted by the relation taking flow partitioning into account [11] are about 15 pct *lower* than those predicted by the Kozeny-Carman relation for these experiments. As can be observed in Figure 6(b), this tendency is confirmed by the experiment, although the measured permeabilities are lower than both predictions.

Experiments (d) through (g) are all in fairly good agreement with the relation in Reference 11 and with the Kozeny-Carman relation (Figure 6). In these cases, the two relations differ by less than 7 pct. It should, however, be noted that the relation in Reference 11 is always closer to the experimental results. The microstructures in these experiments all have low flow partition coefficients (4 to 6 pct), which indicates that the interdendritic liquid is almost immobile. Thus, it is the fraction and length scale of the envelope ($g_e$ and $S_e$) that determine the permeability, rather than the fraction and length scale of the solid phase ($g_s$ and $S_s$). This can be illustrated by setting $g_s$=$g_e$ and $S_s$=$S_e$ for these experiments and thereby neglecting the interdendritic flow. Calculating the permeability using the relation in Reference 11 for the resulting globular morphologies, the values are lowered by only 10 pct with respect to the values for the true morphologies. It appears that the interdendritic liquid contributes very little to the total flow through mushy zones with morphologies similar to those in experiments (d) through (g), at least for solid fractions less than 0.75.

In the microstructure of experiment (h), the high solid fraction ($g_s$=0.83) causes the extradendritic channels to be only slightly wider than the interdendritic channels, as can be observed in Figure 4, experiment (h). For this morphology, the relation in Reference 11 predicts a flow partition coefficient of 14 pct and a permeability 20 pct lower than the Kozeny-Carman relation. As seen in Figure 6(b), this prediction is confirmed by the measured permeability.

Experiment (i) was the one successful out of three attempts to measure on sample 7. This result is particularly interesting since it proves that liquid flow can occur in mushy zones even when the solid fraction is as high as 0.91.

The Kozeny-Carman relation is commonly used in mathematical modelling of flow phenomena during solidification, where the solid fraction is a field variable and the specific surface area of solid is assumed to be constant during solidification. However, the analytical work in Reference 11 along with previous experimental validation and the present work, indicates that a better description of the permeability in a coherent mushy zone can be obtained by considering the effect of both interdendritic and extradendritic flow. It should be noted that in order to improve the permeability model in macrosegregation models like that in Reference 16, an implementation of the relation proposed by Wang *et al.* [11] has to be accompanied by a growth model describing the evolution of the solid morphology.

# Conclusions

- An experimental apparatus for measuring the mushy zone permeability of aluminium-copper alloys with equiaxed microstructures has been constructed. The apparatus is capable of detecting differences in permeability resulting from very

small differences in microstructural morphology.

- Permeability measurements were performed for high solid fractions on a series of Al-Cu alloys with equiaxed microstructures.
- A microstructure characterisation on both the interdendritic and extradendritic length scales accompanies each experiment, and the experimental results are compared to results obtained by relations between the permeability and parameters characterising the solidifying microstructure.
- The measurements constitute experimental validation of the model presented by Wang *et al.* [11].

## Acknowledgements

The authors want to thank Dag Mortensen and Hallstein Hemmer at Institutt for Energiteknikk (Kjeller, Norway), for suggesting and performing the electron-beam welding, which lead to a break-through in the work with the experimental procedure. We are also grateful to Dr. Einar Haug, SINTEF Applied Mathematics, for carrying out the two-dimensional modelling in Appendix B.

The present work was funded by the Brite-EuRam project EMPACT with Project No.BE-1112 and Contract No.BRPR-CT95-0112, and with the following partners: Hoogovens Corporate Services BV (The Netherlands); Hydro Aluminium AS (Norway); Elkem Aluminium ANS (Norway); Pechiney Recherche (France); Vereinigte Aluminiumwerke AG (Germany); Alusuisse-Lonza Services AG (Switzerland); Calcom SA (Switzerland); Technische Universiteit Delft (The Netherlands); Institut National Polytechnique de Lorraine (France); and Ecole Polytechnique Federale de Lausanne (Switzerland). SINTEF together with the Norwegian University of Science and Technology participate in the EMPACT Project as a major sub-contractor to Hydro Aluminium AS and Elkem Aluminium ANS. The authors thank the EMPACT partners and the European Commission for financial support.

## Nomenclature

| | |
|---|---|
| $A$ | cross-sectional area of float and sample channel, mm$^2$ |
| $d$ | grain size, $\mu$m |
| $D$ | diameter of cylinder, mm |
| $g$ | acceleration due to gravity, m/s$^2$ |
| $g_s$ | volume fraction of the solid phase |
| $g_e$ | volume fraction of the grain envelopes |

$H_0$ initial metallostatic height of flux melt, mm
$K$ permeability, $m^2$
$L_A$ perimeter of the solid-liquid interface in an image, $\mu$m
$L_e$ Effective mushy zone length, mm
$L_v$ Effective mushy zone height, mm
$m_f$ mass of float-sensor system, g
$P$ local pressure, Pa
$P_{ext}$ applied gas pressure, Pa
$\Delta P$ pressure difference, Pa
$S_V$ specific surface area of the solid-liquid interface, $m^{-1}$
$S_s$ solid-liquid interfacial area concentration, $m^{-1}$
$S_e$ envelope-liquid interfacial area concentration, $m^{-1}$
$t$ time, s
$V$ superficial velocity, m/s
$X$ float position, m or mm
$\bar{X}$ average float height during measurement, mm
$X_0$ initial float position, mm
$\kappa_v$ flow partition coefficient
$\lambda_2$ secondary dendrite arm spacing, $\mu$m
$\rho_l$ melt density, $kg/m^3$
$\mu_l$ melt viscosity, kg/ms
$\phi_e$ sphericity of the grain envelopes

# Appendix A: Analysing flow in the permeameter

As shown by Poirier and Ganesan [6], the one-dimensional form of Darcy's law generally provides a good description of the flow in this type of experiment because the flow is creeping and the wall effect or Brinkmann term is negligible. However, the permeameter design with the narrow horizontal outlet channel connected to the wider vertical sample channel (Figure 1) chosen to efficiently hold the mushy zone piece in place during the experiment complicates the situation somewhat. In the part of the mushy zone close to the outlet, the average velocity of the flowing liquid changes direction 90 deg and converges to the narrower horizontal channel. In order to account for this effect, the permeameter geometry (see Figure 7(a)) was modelled by a quasi one-dimensional geometry consisting of a vertical section with the length $L_v$=47.5mm and the diameter $D_v$=10.0mm with a short narrower section with length $L_c$ and diameter $D_c$ attached to the outlet end, as shown in Figure 7(b).

For a one-dimensional system, Darcy's law can be written

$$\frac{dP}{dx} = -\frac{\mu_l V(x)}{K} + \rho_l g \tag{A1}$$

where $P$ is the local pressure and $V$ is the superficial velocity. The quantities $\mu_l$ and $\rho_l$ are the viscosity and density of the flux melt, respectively, and $g$ is the acceleration due to gravity. Integrating Eq. (A1) for the geometry in Figure 7(b) from $x$=0 to $x$=$(L_v+L_c)$, assuming constant permeability, gives

$$\Delta P = P(0) - P(L_v + L_c) = \frac{\mu_l}{K}\left[\int_0^{L_v} V dx + \int_{L_v}^{L_v+L_c} V_c dx\right] - \rho g L_v \tag{A2}$$

where $V$ and $V_c$, the superficial velocities in the long and short section, respectively, are related due to mass conservation:

$$V \cdot \frac{\pi D_v^2}{4} = V_c \cdot \frac{\pi D_c^2}{4} \tag{A3}$$

Eq. (A2) can now be written as

$$V = \frac{K}{\mu_l L_e}(\Delta P + \rho_l g L_v) \tag{A4}$$

where $L_e$=$L_v$+$(D_v^2/D_c^2)L_c$ is the effective mushy zone length. Solving Eq. (A4) for $K$ gives Eq. (4) in Section 3.

In order to determine the best choice of the length, $L_c$, and diameter, $D_c$, of the short section in Figure 7(b), a calculation of the two-dimensional flow field in the rectangular geometry shown in Figure 7(a) was performed, using the model presented in Reference 16. The width of the horizontal outlet channel was assumed to be 25 pct of the width of the vertical channel, $D_v$, because this is the ratio between the outlet cross-sectional area and the vertical cross-sectional area in the real three-dimensional system. A case study was defined by choosing a reasonable pressure difference and permeability. The two-dimensional velocity field was calculated and the volume flow rate out of the mushy zone was found by integrating the horizontal component of the velocity at the outlet. This result is compared with the previously derived analytical solution for the one-dimensional model in Figure 7(b). With the choice $D_c$=7.5 mm and $L_c$=5 mm, the volume flow rate, $(V\pi D_v^2/4)$, for a given $\Delta P$ and $K$ in the one-dimensional model is within 2 pct of the result obtained with the two-dimensional model, which is considered satisfactory.

# Appendix B: Permeability relation from Reference [11]

Table 4 lists the equations in the permeability relation suggested by Wang *et al.* [11]. The necessary input to the relation are $g_s$, $S_s$, $g_e$, $S_e$, and $\phi_e$, as defined in the Nomenclature. The limit $g_e = 0.3$ in Eq. (B5) is a rough estimate of the dendritic coherency point, i.e., the transition between freely moving crystals and a coherent solid network.

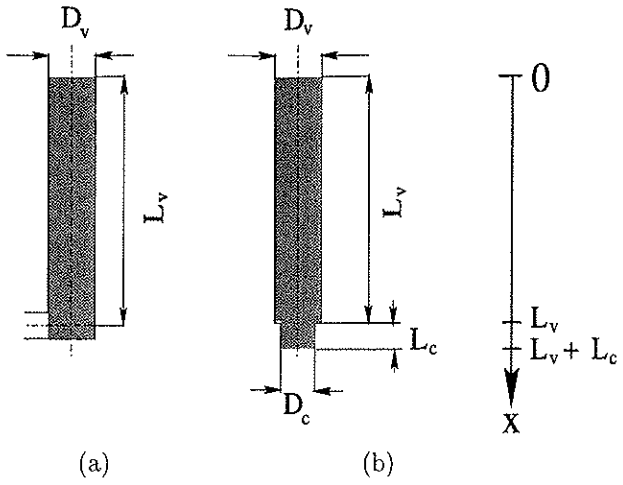


Figure 7: *(a) Permeameter geometry. (b) Quasi one-dimensional model used to represent (a).*

Table 4: *The equations in the permeability relation presented in Reference [11].*

| | | |
|---|---|---|
| *Permeability:* | $K = \frac{1}{S_e^2}\left[\frac{3g_e}{\phi_e\beta}\right]^2$ | (B1) |
| *General correlation:* | $\beta = \frac{\beta_d}{[g_e^n+(\beta_d/\beta_l)^{2n}]^{1/2n}}, \quad n = 0.176\log_{10}\beta_d + 0.275$ | (B2) |
| *Interdendritic permeability:* | $\beta_d = \frac{3\sqrt{5}}{(1-g_s/g_e)^{3/2}}\frac{S_s}{\phi_e S_e}$ | (B3) |
| *Extradendritic permeability:* | $\beta_l = \left\{\frac{9}{2}g_e\frac{2+\frac{4}{3}g_e^{5/3}}{2-3g_e^{1/3}+3g_e^{5/3}-2g_e^{6/3}}\frac{1}{C_p(\phi_e)}\frac{2\beta_d^2[1-\tanh(\beta_d)/\beta_d]}{2\beta_d^2+3[1-\tanh(\beta_d)/\beta_d]}\right\}^{1/2}$ | (B4) |
| *Grain shape function:* | $C_p(\phi_e) = \begin{cases} \phi_e^2 & : \ 0.3 < g_e < 1 \\ 1.26\log_{10}\left(\frac{\phi_e}{0.163}\right) & : \ 0 < g_e < 0.3 \end{cases}$ | (B5) |
| *Flow partition coefficient:* | $\kappa_v = g_e\left(\frac{\beta}{\beta_d}\right)^2$ | (B6) |

# References


[1] P. C. Carman. *Flow of gases through porous media*, pages 11–13. Butterworth Scientific, London, 1956.

[2] T. S. Piwonka and M. C. Flemings. Pore formation in solidification. *Transactions of the Metallurgical Society of AIME*, **236**:1157–1165, 1966.

[3] C. J. Paradies, L. Arnberg, H. J. Thevik, and A. Mo. Permeabilities for interdendritic melt flow through equiaxed aluminium castings. In M. Cross and J. Campbell, editors, *Modeling of casting, welding and advanced solidification processes VII*, pages 609–616. TMS, Warrendale, PA, 1995.

[4] N. Streat and F. Weinberg. Interdendritic fluid flow in a lead-tin alloy. *Metallurgical Transactions B*, **7B**:417–423, 1976.

[5] K. Murakami and T. Okamoto. Fluid flow in the mushy zone composed of granular grains. *Acta Metallurgica*, **32**:1741–1744, 1984.

[6] D. R. Poirer and S. Ganesan. Permeabilities for flow of interdendritic liquid in equiaxial structures. *Materials Science and Engineering*, **A157**:113–123, 1992.

[7] D. R. Poirer and P. Ocansey. Permeability for flow of liquid through equiaxial mushy zones. *Materials Science and Engineering*, **A171**:231–240, 1993.

[8] P. Ocansey, M. S. Bhat, D. R. Poirier, and T. L. Finn. Permeability for liquid flow in the mushy zones of equiaxed castings. In U. Mannweiler, editor, *Light Metals 1994*, pages 807–812. TMS-AIME, Warrendale, PA, 1994.

[9] S. Viswanathan, A. J. Duncan, A. S. Sabau, and Q. Han. Prediction of microporosity in aluminium. In B. G. Thomas and C. Beckermann, editors, *Modeling of casting, welding and advanced solidification processes VIII*, pages 849–856. TMS, Warrendale, PA, 1998.

[10] C. Y. Wang and C. Beckermann. A multiphase solute diffusion model for dendritic alloy solidification. *Metallurgical Transactions A*, **24A**:2787–2802, 1993.

[11] C. Y. Wang, S. Ahuja, C. Beckermann, and H. C. de Groh III. Multiparticle interfacial drag in equiaxed solidification. *Metallurgical and Materials Transactions B*, **26B**:111–119, 1995.

[12] E. E. Underwood. *Quantitative Stereology*, page 24. Addison-Wesley, 1970.

[13] D. R. Poirier, S. Ganesan, M. Andrews, and P. Ocansey. Isothermal coarsening of dendritic equiaxial grains in Al-15.6% Cu alloy. *Materials Science and Engineering*, **A148**:289–297, 1991.

[14] S. Ganesan, R. Speiser, and D. R. Poirier. Viscosities of aluminum-rich Al-Cu liquid alloys. *Metallurgical Transactions B*, **18B**:421–424, 1987.

[15] S. Ganesan and D. R. Poirier. Densities of aluminum-rich aluminum-copper alloys during solidification. *Metallurgical Transactions A*, **18A**:721–723, 1987.

[16] J. Happel. Viscous flow in multiparticle systems: Slow motion of fluids relative to beds of spherical particles. *American Institute of Chemical Engineers Journal*, **13**:122–125, 1958.

[17] H. J. Thevik and A. Mo. The influence of micro-scale diffusion and dendrite coarsening upon surface macrosegregation. *International Journal of Heat and Mass Transfer*, **40**:2055–2065, 1997.

[18] H. J. Thevik, A. Mo, and T. Rusten. A mathematical model for surface segregation in aluminium DC casting. *Metallurgical and Materials Transactions B*, **30B**:135–142, 1999.

# Article 2:

# Experimental difficulties associated with permeability measurements in aluminium alloys

Øyvind Nielsen* Lars Arnberg*

**Abstract**

General principles and experimental difficulties associated with the measurement of permeability in aluminium alloys have been discussed in order to ease a further development of experimental methods suitable for such measurements. In order to avoid the surface tension effects associated with liquid/gas interfaces in the narrow channels of the mushy zone, a flux melt can be used at the inlet of the permeameter. Electron-beam welding has been shown to be a suitable method for ensuring a complete wetting between sample and flux after remelting to the test temperature. Moreover, the influence of the permeameter design and the experimental procedure on grain detachment, preferred flow channel formation, and coarsening have been revealed through microstructure images.

*Department of Materials Technology and Electrochemistry, Norwegian University of Science and Technology, 7491 Trondheim, Norway

# 1 Introduction

The Kozeny-Carman relation along with more recent theory [1] are in fairly good agreement with the permeability measurements of equiaxed aluminium alloys presented in the literature [2]. However, because the existing data are scarce, there is still a need for validation of these relations for a large range of alloys and morphologies. The permeability measurements have been presented with little or no discussion about the considerable experimental difficulties associated with the experiments [2–5]. Therefore, it can be difficult for others to reproduce these measurements and to use the suggested experimental methods to measure the permeability for other alloys and morphologies.

In the present article we will discuss some of the experimental difficulties associated with the measurement of mushy zone permeability in aluminium alloys, based on the experience gained through the work with the development of the experiment presented in Reference [2]. General experimental principles are discussed. Furthermore, the concept of a flux material is described, and the influence of the permeameter design and the experimental procedure on grain detachment, preferred flow channel formation, and coarsening is revealed through microstructure images.

# 2 Experimental principles

The interdendritic liquid flow through a mushy zone with a rigid or 'coherent' solid phase is commonly described by Darcy's law. In differential form, this law can be written

$$\nabla p = -\frac{\mu_l \vec{V}}{K} + \rho_l \vec{g} \tag{1}$$

where $p$ is the local pressure, $\vec{V}$ is the superficial liquid velocity (local volume averaged liquid velocity times the liquid fraction), and $K$ is the permeability. The quantities $\mu_l$ and $\rho_l$ are the viscosity and the density of the interdendritic liquid, respectively, and $\vec{g}$ is the acceleration due to gravity.

For a homogeneous mushy sample in a cylindrical container (Figure 1), integration of the one dimensional version of Eq. (1) along the centreline of the cylinder yields

$$p_{ext} = \frac{\mu_l V L}{K} - \rho_l g L \quad \text{or} \quad K = \frac{\mu_l V L}{p_{ext} + \rho_l g L} \tag{2}$$

where $p_{ext}$ is an applied pressure and $L$ is the length of the mushy sample.[1] Figure 1 along with Eq. (2) reveals the principle of a permeameter: if we set up a pressure difference over a one dimensional mushy zone and measure the resulting superficial liquid velocity, we can calculate the permeability from Eq. (2).

[1] If the cylinder is horizontally aligned, the term containing $\vec{g}$ in Eq. (2) disappears.

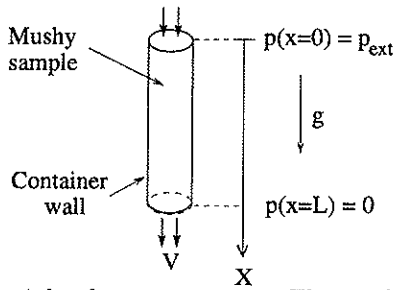


Figure 1: *The general principle of a permeameter. The symbol $p$ represents the applied pressure, $V$ is the superficial liquid velocity, $L$ is the mushy sample length, and $g$ is the acceleration due to gravity.*

Measurement of the superficial liquid velocity in a permeameter requires a finite displacement of the liquid relative to the coherent solid phase. Thus, a pressurised fluid, a flux, must enter the mushy sample at one end of the permeameter, forcing the liquid to exude on the other end. If a liquid flux is chosen, i.e., a flux melt, the surface tension effects associated with liquid/gas interfaces in the narrow channels of the solid network can be avoided. Moreover, if the flux melt has the same composition as the interdendritic liquid, constitutional remelting/solidification is minimised. The use of other types of fluxes could introduce errors in the permeability measurements if the effects of surface tension and/or remelting/solidification are not accounted for in the data analysis.

A possible experimental goal is to measure the permeability of an alloy at a constant temperature and to correlate permeability with microstructural quantities. In this case, it is necessary to obtain a quantitative stereological characterisation of the solid phase morphology. This has been achieved by quenching of the mushy sample during the permeability experiment and subsequent metallography and image analysis which distinguish between the phases which were solid and liquid during the experiment. It should be emphasised that quenching of aluminium alloys only in special cases gives the desired metallographical contrast between the solid and liquid phases [6–8]. This is one of the reasons why permeability measurements with corresponding morphology characterisation are so far only reported for binary alloys where the interdendritic liquid has eutectic composition [2–5].

Another possible experimental goal is to measure the permeability and the temperature of an alloy during solidification/remelting and to correlate the permeability with the solid fraction, which can be estimated from the temperature-time curves. In this case, the composition of the interdendritic liquid will vary throughout the experiment which complicates the experimental design, the experimental method, and the data analysis. This type of experiment along with a modelling concept capable of extracting reliable permeabilities from the measurements has not been presented. Therefore, only constant

temperature permeability measurements will be discussed in this article.

# 3 The experiment

## 3.1 The flux alloy

For a constant temperature permeability measurement, the composition of the interdendritic liquid in the alloy sample at the chosen test temperature can be estimated e.g., from the phase diagram. If a flux alloy with this composition is used, the test temperature will equal the liquidus temperature of this flux alloy.

Before the start of the measurement, the mushy sample must be brought to the test temperature and be joined with the flux melt. Because the flux melt is to penetrate into the mushy sample it is essential to obtain a complete wetting between the sample surface and the flux melt. In the work with the development of the experimental setup presented in Reference [2], this turned out to be a major technical problem due to the formation of oxide layers on the sample and flux surfaces, which prevented the flow. The problem was solved by electron-beam (EB) welding of the two alloys and remelting of the joined sample–flux piece to the test temperature. The details concerning the procedure has recently been presented elsewhere [2], but some images of the welding zone will be discussed subsequently in order to reveal why the electron-beam welding solution is satisfactory.

Figure 2 shows the as-welded joint between the as-cast mushy sample and the flux alloy prior to remelting. The welding zone varies in width from about 3 mm at the surface of the sample to about 1 mm in the centre. The composition of the weld is between the compositions of the sample and the flux alloy and the microstructure is very fine due to the rapid cooling in the EB-welding process. Figure 3 shows the welded joint after the permeability experiment in two different cases. For the large grained dendritic sample (Figure 3(a)), the welding zone is completely washed away by convection in the flux melt and can be seen as scattered globular grains in the upper left corner of the image. Thus, in this case, the welding zone represents no resistance to the flow of flux melt into the mushy sample. For the smaller grained sample (Figure 3(b)), the welding zone is only partly washed away. However, large channels through the welding zone are formed by which the flux melt can flow freely into the mushy sample.

## 3.2 Permeameter design

In order to be able to describe the flow in a permeameter by Darcy's law, the permeameter design and the sample morphology must be such that: (*i*) movement of the solid phase relative to the permeameter is avoided, and (*ii*) the formation of preferential flow channels

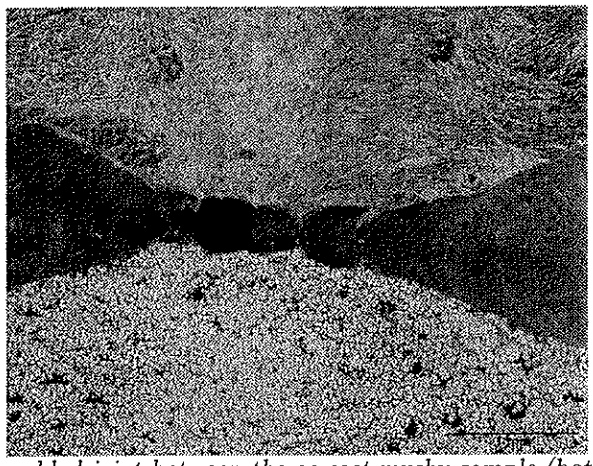

Figure 2: *The as-welded joint between the as-cast mushy sample (bottom) and the flux alloy (top). The welding zone varies in width from about 3 mm at the surface of the sample to about 1 mm in the centre.*

is avoided. These conditions will be discussed subsequently.

Different methods have been used in order to avoid movement of the solid phase relative to the permeameter. Poirier and Ganesan [3] used a horizontal sample held in place only by a tight fit with the cylindrical channel, as shown in Figure 4(a). Duncan *et al.* [5] used a threaded horizontal sample which was screwed into a channel and sealed with ceramic cement to avoid preferential flow along the tapped wall (Figure 4(b)). Nielsen *et al.* [2] used a vertical sample with a horizontal outlet from the sample end (Figure 4(c)). Even though these solutions can prevent the movement of the coherent solid phase, they can not prevent the detachment of grains at the outlet of the mushy sample. Examples of the microstructure at the outlet in the experiment presented in Reference [2] are shown in Figure 5. Grain detachment is observed in samples with grains which are small compared with the outlet and which have a globular morphology (Figure 5(a)). On the other hand, large grained samples with a dendritic morphology show little or no tendency for grain detachment (Figure 5(b)).

For a given sample morphology, the tendency for grain detachment at the outlet and formation of preferential flow channels along the permeameter wall and in the bulk of the sample depends on the local pressure gradient. For a homogeneous sample, the pressure gradient is equal to the ratio between the applied pressure and the sample length. In the permeameter shown in Figure 4(c), preferential flow was observed for globular morphologies when the pressure gradient exceeded a value of 50 kPa/m (Figure 6). For larger grained dendritic of 'clover-leaf' morphologies, pressure gradients as high as 200 kPa/m were used without problems.

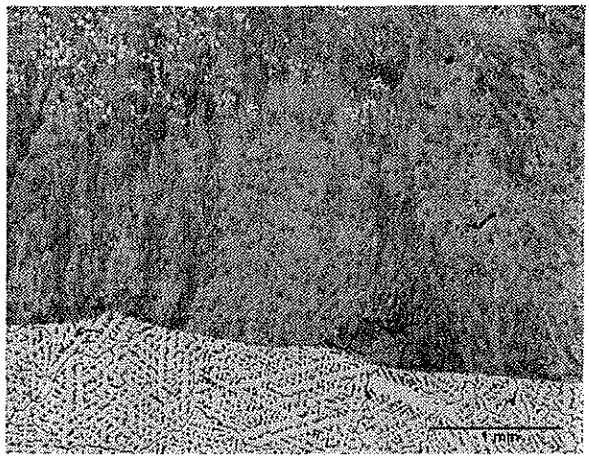

(a) A case where the grains of the welding zone are completely washed away from the sample/flux interface

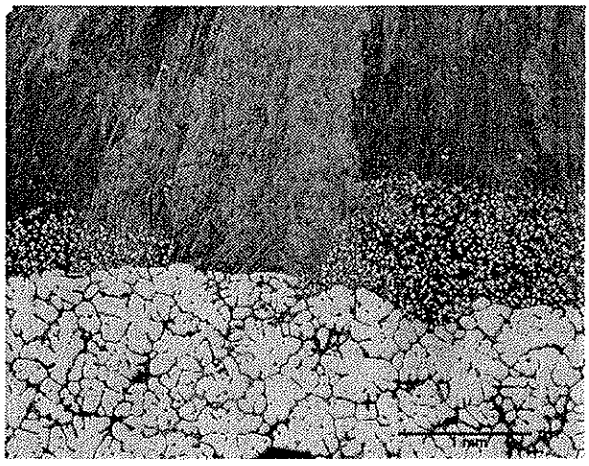

(b) A case where a wide channel is formed through the welding zone

Figure 3: *The boundary between the mushy sample (bottom) and the flux alloy (top) during the permeability measurement in two different cases.*

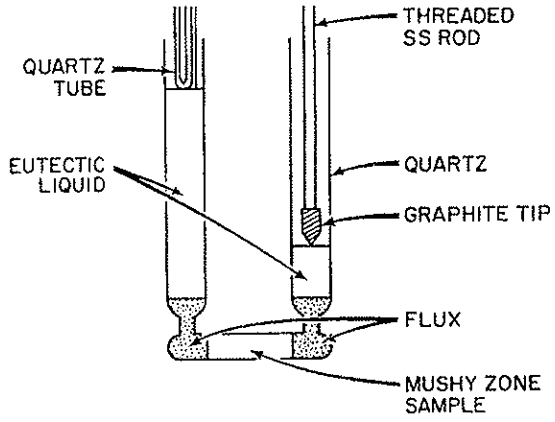


(a) Horizontal sample held in place only by a tight fit with the cylindrical channel [3]

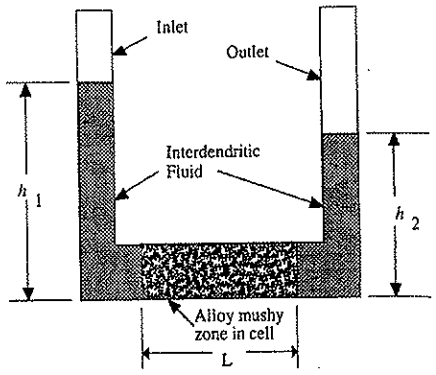


(b) Horizontal sample with threads screwed into the cylindrical channel [5]

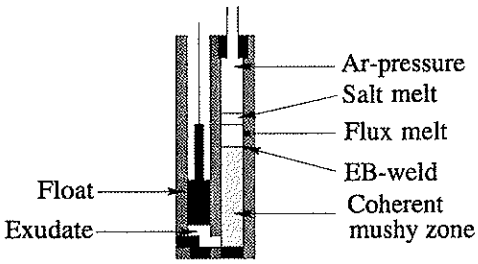


(c) Vertical sample with horizontal outlet [2]

Figure 4: *Different methods for avoiding movement of the solid phase relative to the permeameter.*

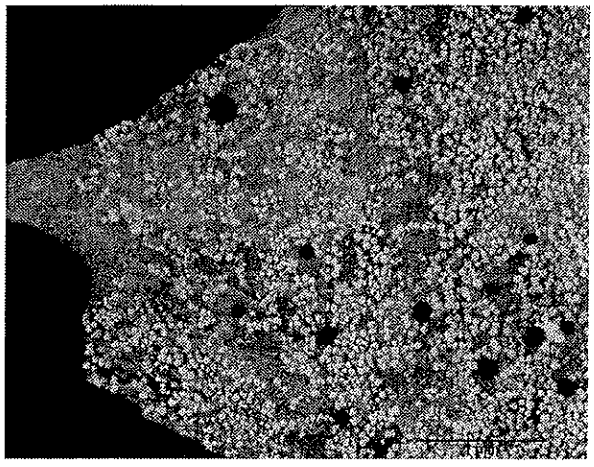

(a)

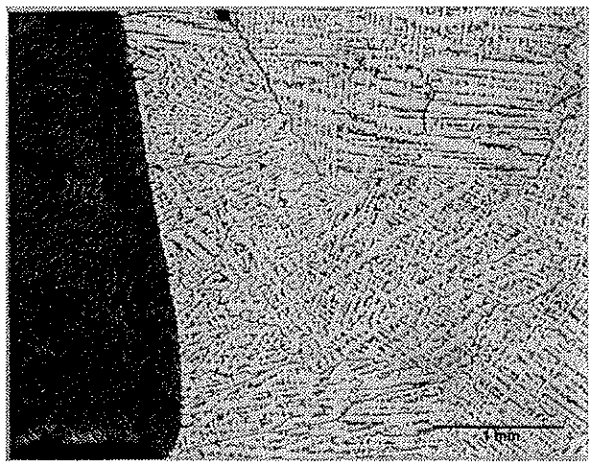


(b)

Figure 5: *The outlet of the permeameter for: (a) a globular mushy zone sample where severe solid movement is observed, and (b) a dendritic mushy zone sample where no solid movement is observed. Solid movement results in failure of the assumptions involved in the application of Darcy's law. The mushy zone extends towards the right and upwards in both micrographs.*

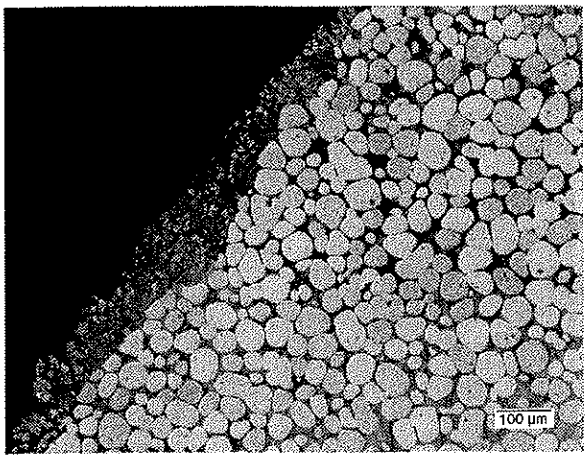


Figure 6: *Preferred flow channel formed at the container wall (upper left) during a permeability measurement.*

## 3.3 Coarsening and globularisation in the mushy sample

In the constant temperature permeability measurements presented in the literature [2–5], the samples were remelted and remained in the mushy zone for several minutes. The rate of coarsening and globularisation during this time increases with decreasing grain size and 'cell' or secondary dendrite arm spacing [9]. For the Al-Cu alloys used in Refs. [2–5], a significant coarsening and globularisation was observed in all the cases. This is revealed in Figure 7 for the experiment presented in Reference [2]. These microstructural changes have at least two important consequences which will be discussed subsequently.

For the modelling of interdendritic fluid flow in casting processes, we need permeability measurements for the different types of morphology which forms during casting under different conditions. Since the time available for coarsening and globularisation in the experiments are much longer than in a typical casting process, the morphology in the experiments will, however, be significantly different from the morphology which develops during casting. Thus, the use of e.g., the Kozeny-Carman relation, which has been validated by permeability measurements, in interdendritic fluid flow modelling involves an extrapolation of the experimental results.

If the morphology did not change with time during an experiment, the as-cast morphology could be correlated directly with the measured permeability. In reality, due to the coarsening and globularisation, the sample must either be quenched during the experiment to reveal the morphology, [2,3] or the microstructural changes with time must be assessed from separate isothermal coarsening experiments. The latter method is, however, not reliable because the fluid flow during the experiment, which would not be

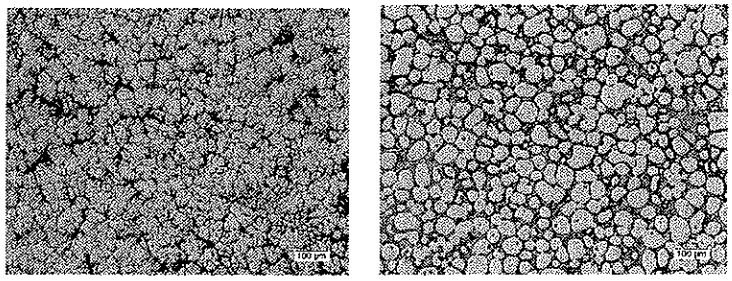

(a) Left: As-cast microstructure. Right: Microstructure during the permeability measurement.

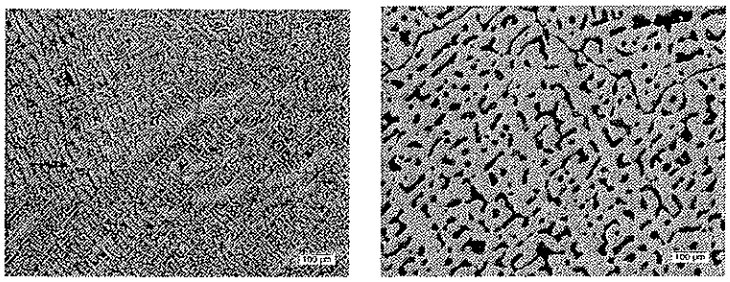

(b) Left: As-cast microstructure. Right: Microstructure during the permeability measurement.

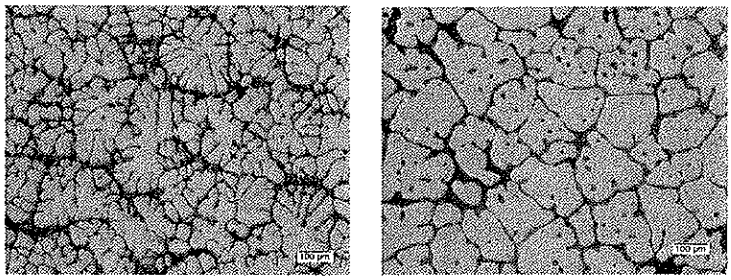

(c) Left: As-cast microstructure. Right: Microstructure during the permeability measurement.

Figure 7: *The microstructures in the as-cast state and after a permeability experiment in three different cases revealing the effect of the coarsening during the experiment.*

present in the separate isothermal coarsening experiments, has been shown to influence the coarsening [5]. The quenching method works well provided that the interdendritic liquid has eutectic composition, but the method is limited by the fact that only one data point is obtained for each experiment.

As shown by Poirier and Ganesan [9], the coarsening rate in a typical Al-Cu alloy used in the permeability experiments is very high during the first minute after the start of remelting and then decreases rapidly. This was utilised in Reference [2] where it was shown that if (*i*) the measurement is started after the initial period of rapid coarsening, and (*ii*) the total measurement time is kept low (~50 s), the permeability remains constant during the measurement.

# Conclusions

General principles and experimental difficulties associated with the measurement of permeability in aluminium alloys have been discussed in order to ease a further development of experimental methods suitable for such measurements. The main results of the discussion can be summarised as follows:

- In order to avoid the surface tension effects associated with liquid/gas interfaces in the narrow channels of the mushy zone, a flux melt can be used at the inlet of the permeameter.
- Electron-beam welding is a suitable method for ensuring a complete wetting between sample and flux after remelting to the test temperature.
- By using a test temperature just above the eutectic temperature of the alloying system, the grain morphology corresponding to the measured permeability can be assessed by quenching during a measurement.
- Due to coarsening and globularisation of the sample during the permeability measurement, the grain morphology corresponding to the measured permeability is significantly different from the grain morphology which forms during solidification in a typical casting process.

# References

[1] C. Y. Wang, S. Ahuja, C. Beckermann, and H. C. de Groh III. Multiparticle interfacial drag in equiaxed solidification. *Metallurgical and Materials Transactions B*, **26B**:111–119, 1995.

[2] Ø. Nielsen, L. Arnberg, A. Mo, and H. Thevik. Experimental determination of the mushy zone permeability in Al-Cu alloys with equiaxed microstructures. *Metallurgical and Materials Transactions A*, **30A**:2455–2462, 1999.

[3] D. R. Poirer and S. Ganesan. Permeabilities for flow of interdendritic liquid in equiaxial structures. *Materials Science and Engineering*, **A157**:113–123, 1992.

[4] P. Ocansey, M. S. Bhat, D. R. Poirier, and T. L. Finn. Permeability for liquid flow in the mushy zones of equiaxed castings. In U. Mannweiler, editor, *Light Metals 1994*, pages 807–812. TMS-AIME, Warrendale, PA, 1994.

[5] A. J. Duncan, Q. Han, and S. Viswanathan. Measurement of liquid permeability in the mushy zones of aluminum-copper alloys. *Metallurgical and Materials Transactions B*, **30B**:745–750, 1999.

[6] S. W. Chen and C. C. Huang. Solidification curves of Al-Cu, Al-Mg and Al-Cu-Mg alloys. *Acta Materialia*, **44**:1955–1965, 1996.

[7] A. M. Figuerdo, Y. Sumartha, and M. C. Flemings. Measurement and calculation of solid fraction in quenched semi-solid melts of rheocast aluminium alloy A357. In *Light Metals 1998*, pages 1103–1106. TMS-AIME, Warrendale, PA, 1998.

[8] Ø. Nielsen, B. Appolaire, H. Combeau, and A. Mo. Measurements and modeling of the microstructural morphology during equiaxed solidification of Al-Cu alloys. *Submitted to the Metallurgical and Materials Transactions*, January, 2000.

[9] D. R. Poirier, S. Ganesan, M. Andrews, and P. Ocansey. Isothermal coarsening of dendritic equiaxial grains in Al-15.6% Cu alloy. *Materials Science and Engineering*, **A148**:289–297, 1991.

# Article 3:

# Measurements and modelling of the microstructural morphology during equiaxed solidification of Al-Cu alloys

Ø. Nielsen* B. Appolaire† H. Combeau† A. Mo‡

**Abstract**

The morphology predicted by an equiaxed growth model recently presented elsewhere has been compared with quantitative experimental morphology measurements on a range of Al-Cu alloys. In the experiments, the samples have been solidified with uniform temperature and quenched from the mushy state at the instant when the eutectic temperature was reached. The copper content and the amount of grain refiner additions have been varied, resulting in both 'clover-leaf' and dendritic equiaxed morphologies. Morphology characterisation on both the intragranular and extragranular length scales has been performed on the quenched samples. Average heat extraction rates, grain densities, and alloy compositions from the experiments have been used as input to the equiaxed grain growth model, and the resulting morphology predictions have been compared with the morphology measurements. For the morphologies observed in the present study, the equiaxed growth model predicts higher values of the internal solid fraction than observed experimentally. This has been indicated to be due to the failure of commonly made modelling assumptions during the later stages of the solidification.

*Department of Materials Technology and Electrochemistry, Norwegian University of Science and Technology, 7491 Trondheim, Norway

†Ecole des Mines de Nancy, Parc de Saurupt, F-5404 Nancy Cedex, France

‡SINTEF Materials Technology, P. O. Box 124, Blindern, 0314 Oslo, Norway

# 1 Introduction

Because the quality of cast products is to a great extent controlled by the solidification conditions, the production of good castings requires a basic knowledge of the mushy zone. This zone is characterised both by its microstructural morphology and by properties observed on the macroscopic scale such as dendrite coherency and permeability to interdendritic melt flow. The parameters entering on the micro and macro scales are furthermore interrelated. An example is revealed in the mathematical modelling of macrosegregation formation. In this case, the momentum equation contains a solid/liquid interfacial drag term (i.e., the permeability) which has been suggested to depend on the local morphology in terms of the volume fraction of solid, the specific surface of the solid, the volume fraction and specific surface of the grain envelopes, and the average envelope shape factor [1, 2]. The microstructural morphology is, on the other hand, influenced by conditions given at the macroscopic level, such as the alloying, the inoculation, and the cooling conditions.

In micro-macro modelling of equiaxed solidification of Al alloys (e.g., Refs. [3,4]), the development of the microstructural morphology is commonly estimated by models which describe the solidification as a result of micro-scale phenomena [5–10]. These models rely on simplifications of the real microstructure and on the separation of different length scales. Due to a lack of experimental investigations on equiaxed morphology development, these micro-models have not yet been quantitatively validated for Al alloys. Moreover, a dendritic morphology is assumed in the modelling of the grain envelope growth and of the solid surface development. A 'clover-leaf' morphology is, however, observed in the as-cast microstructures of well grain refined Al alloys. This type of morphology has been suggested to result from some kind of cellular growth [11]. A comparison between the morphology predicted by the models in Refs. [5–10] and experimental morphology characterisation for this type of equiaxed microstructure has not been reported.

A standard experimental technique for morphology investigations is to interrupt the solidification process by quenching. This procedure relies on the assumption that the liquid remaining at the instant of quenching will solidify with a morphology sufficiently different from the already solidified microstructure to be quantitatively distinguished by metallography. In two recent works [12, 13], the development of the solid fraction during growth of primary aluminium was measured for different alloys using this quenching technique. Compared to the Scheil equation, the lever rule, and DTA measurements, the results systematically overestimated the calculated solid fraction, which indicate that the change in the heat extraction rate at the quenching point did not produce an instantaneous discernible change in the growth morphology. This tendency is qualitatively confirmed by images of microstructures of industrial aluminium alloys quenched at dendrite coherency, as reported by Arnberg *et al.* [14]. Consequently, conventional quenching

experiments can not be considered reliable for quantitative morphology characterisation.

The quenching method can, however, be considered reliable at the instant when the remaining melt reaches the eutectic composition, as demonstrated in several works aiming at correlating microstructural morphology with permeability for Al-Cu alloys [2, 15–17]. When an Al-Cu alloy is quenched at this instant, the remaining melt will solidify as a very fine Al-$Al_2Cu$ eutectic which is easily discernible from the primary Al phase. Thus, the distribution of eutectic inside the grain envelopes (intragranular) and between the grain envelopes (extragranular) can be measured and compared with modelling predictions. It should be noted that even without quenching of the eutectic, an acceptable contrast can be achieved, as utilised by Rappaz and Thévoz [5] for qualitative observations on Al-7 wt.% Si alloys. To the knowledge of the authors, quantitative morphology measurements have not been presented.

The purpose of this article is to present a comparison between the morphology predicted by the equiaxed growth model recently presented in Refs. [9,10] and quantitative experimental morphology investigations on Al-Cu alloys with different morphologies. In the experiments, the Al-Cu samples solidify with uniform temperature and are quenched from the mushy state at the instant when the eutectic temperature is reached. The copper content and the amount of grain refiner addition are varied. The morphology of the quenched samples is characterised on both the intragranular and extragranular length scales. Average heat extraction rates, grain densities, and alloy compositions from the experiments are used as input to the model, and the resulting morphology predictions are compared with the experimental results. Furthermore, the effect of the predicted morphology on the prediction of the mushy zone permeability is discussed.

# 2 Experimental

## 2.1 Procedure

Six binary Al-Cu alloys were prepared in melt batches of $0.5\times10^{-3}\mathrm{m}^3$ from pure aluminium (>99.99%) and copper. Each melt batch was heated to 720°C and inoculated with a certain amount of commercial Al-5 wt.% Ti-1 wt.% B rod master alloy. Prior to each experiment, the melt was stirred with a graphite rod and a sample was taken for spectroscopic chemical analysis.

A sketch of the experimental setup used for the solidification experiments is shown in Figure 1. Prior to each experiment, a cylindrical graphite crucible with 13-mm inner radius and 18-mm height, was pre-heated floating on top of the molten alloy for five minutes. The crucible was then filled with melt and allowed to cool in surroundings at room temperature while the temperature in the solidifying sample was recorded continuously using a 1-mm steel-mantled thermocouple (type K) covered by boron nitride. The

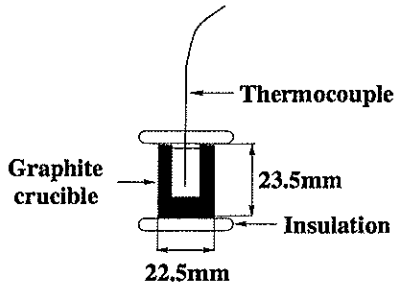


Figure 1: *The experimental setup.*

crucible and sample were quenched at the eutectic temperature (547.7°C) by pouring cold water directly on the top surface of the sample. It was then possible to remove the thermocouple from the quenched samples without remelting of the sample and without destroying the thermocouple.

The thermocouple was calibrated by measuring the solidification plateau of pure aluminium (>99.99%). The plateau temperature was defined to be 660.3°C and the deviation of the thermocouple from this absolute scale was assumed to be constant over the solidification interval of the sample alloys used (547-649°C). The calibration routine was performed before and after each experiment, showing that the measured plateau temperature changed with less than 0.1°C. The same thermocouple was used in all the experiments. The random error in the measuring system has been estimated to ±0.5°C [18].

## 2.2 Metallography and image analysis

The quenched sample from each experiment was cut in a single section along the cylinder axis, mechanically ground, polished down to 1 $\mu$m, and anodised. For each sample, between 10 and 20 areas were randomly selected and two different grey-scale images were recorded from each area:

1. a bright field image to distinguish the quenched Al-$Al_2Cu$ eutectic from the primary Al phase (Figure 2a);

2. a polarised light image to distinguish neighbouring grains (Figure 2b).

From the image recorded with polarised light, the mean linear intercept, $\bar{l}$, was measured for each sample using the linear intercept method. The average centre-to-centre distance between grains, $d$, is related to the mean linear intercept by [19]:

$$d = A\bar{l} \tag{1}$$

where $A$ is a constant with a value between 1.13 and 1.78 depending on the grain shape [19]. Because the grain shape is not readily measured from two-dimensional images, $A =$

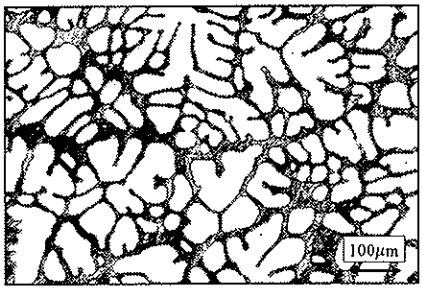


(a) Bright field image

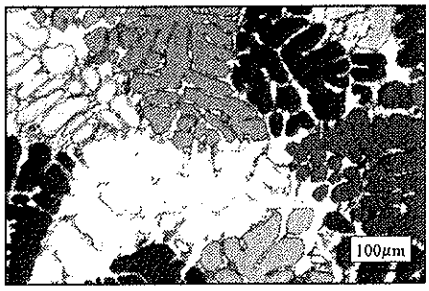


(b) Polarised light image

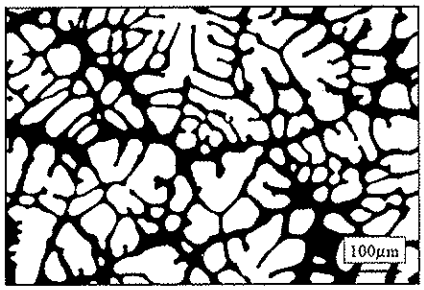


(c) Binary image

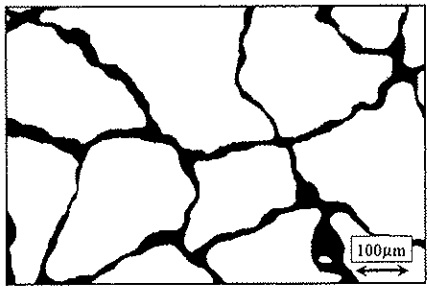


(d) Modified binary image

Figure 2: *Stages in the image analysis process.*

1.5 was applied in the present study. According to Fullman [20], this value corresponds to a spherical grain shape. If we assume that the average available volume for each grain is a sphere with a diameter $d$, the corresponding grain density, $n$, becomes:

$$n = \frac{1}{\frac{4}{3}\pi\left(\frac{d}{2}\right)^3} = \frac{6}{\pi d^3} \tag{2}$$

From the bright field images (Figure 2a), a rough estimate of the average 'cell' or secondary dendrite arm spacing in each sample was found by counting the number of 'cells' or secondary dendrite arms per unit length on selected grains.

In order to quantify the microstructural morphology at the instant when the eutectic temperature was reached, each bright field image was transformed into a binary 'solid–liquid' image (Figure 2c) using automatic image analysis (AIA). From these binary images, the volume fraction of solid, $g_s^E$, and the amount of solid surface per unit volume (solid/liquid interfacial area concentration), $S_s^E$, were measured using AIA. The superscript $E$ is used to represent values at the eutectic temperature.

In order to separate the intragranular and the extragranular liquid phases, the grain envelopes were drawn manually in each binary 'solid–liquid' image. The identification of grains from the individual grain fragments in a two-dimensional image was accomplished by consulting the polarised light image along with the shape of the grain fragments. For example, the large white region in Figure 2b was assumed to consist of two individual grains, based on the shape of the corresponding grain fragments in Figure 2a. From the resulting binary 'envelope–extragranular liquid' image (Figure 2d), the volume fraction of the grain envelopes, $g_e^E$, and the envelope/liquid interfacial area concentration, $S_e^E$, were measured using AIA.

The stereological assumptions and relations needed to calculate the morphological quantities from the quantities provided by the AIA are described in Reference [2]. The final results are reported as the mean value of the measurements on 10 to 20 images with the corresponding standard error in the mean. The volume fraction of solid within the grain envelope, $g_i^E = g_s^E/g_e^E$, hereafter called the internal solid fraction, is also reported for each sample.

It should be emphasised that the image analysis procedure relies on the use of anodising and polarised light to distinguish between neighbouring grains. However, because the anodising amplifies topography effects, obtaining the necessary high contrast bright field images from the samples requires a very careful polishing, short anodising times, and high magnifications.

Table 1: *The samples characterised by the nominal copper content, $w_0$, the titanium and impurity content, the measured grain density, $n^E$, a rough estimate of the 'cell' or secondary dendrite arm spacing, $\lambda_2^E$, and the average heat extraction rate, $\dot{Q}_{exp}$.*

| Sample | $w_0$ [wt.% Cu] | wt.% Ti | wt.% others | $n^E[10^{11}\mathrm{m}^{-3}]$ | $\lambda_2^E[\mu\mathrm{m}]$ | $\dot{Q}_{exp}[10^3\mathrm{J/(kg\ s)}]$ |
|---|---|---|---|---|---|---|
| 1 | 4.70 | 0.017 | $< 0.02$ | 1.08±0.08 | – | 5.6 |
| 2 | 10.0 | 0.009 | $< 0.03$ | 1.5±0.1 | 42 | 5.5 |
| 3A | 14.9 | 0.004 | $< 0.02$ | 0.59±0.08 | 32 | 5.2 |
| 3B | 15.6 | 0.025 | $< 0.03$ | 2.3±0.1 | 39 | 5.0 |
| 4A | 20.1 | 0.003 | $< 0.03$ | 0.18±0.09 | 26 | 5.0 |
| 4B | 19.7 | 0.009 | $< 0.03$ | 1.18±0.08 | 36 | 4.7 |

# 3 Experimental results

The chemical compositions of the samples are given in Table 1 along with the measured grain densities, the estimated 'cell' or secondary dendrite arm spacings, and the average heat extraction rates. It should be noted that the letters A and B in the sample names correspond to low and high grain densities, respectively. The average heat extraction rates, $\dot{Q}_{exp}$, given in Table 1, are determined from the relation

$$\dot{Q}_{exp} = \frac{h(T_{eut}) - h(T_{liq})}{t_{exp}} = \frac{c_p(T_{eut} - T_{liq}) - g_s^E L}{t_{exp}} \tag{3}$$

where $h$ is the specific enthalpy of the sample and $t_{exp}$ is the time required to cool the sample from the liquidus temperature, $T_{liq}$, to the eutectic temperature, $T_{eut}$, as determined from the experimental temperature-time curves. The quantities $c_p$ and $L$ are the specific heat capacity and the specific latent heat of the samples, respectively (Table 3).

Table 2 shows the results from the morphology measurements along with calculated results for the comparison with model predictions to be discussed in Section 5. It can be seen that an increase in the copper content generally decreases the value of the internal solid fraction, $g_i^E$, in the quenched samples, while an increase in the grain density increases $g_i^E$. For the surfaces, $S_s^E$ increases with increasing copper content and grain density, while $S_e^E$ increases with increasing grain density. The solid fraction, $g_s^E$, decreases with increasing copper content as expected and is independent of grain density.

Figure 3 shows representative examples of the morphologies in the quenched samples. Sample 1 (Figure 3a) has a nearly globular morphology ($g_i^E = 0.951$) where individual cells of some kind can be seen but can not be quantitatively distinguished. Samples 2 and 3B (Figure 3b and d), are also quite globular, but in these cases individual 'cells' can easily be distinguished, indicating a separate length scale in the growth mode within the

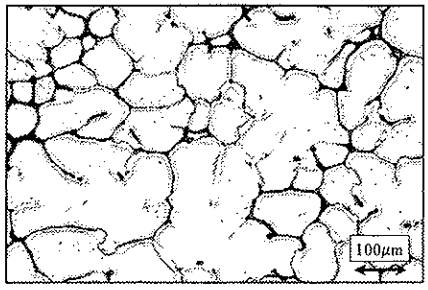


(a) Sample 1

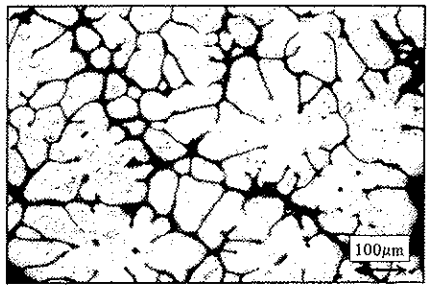


(b) Sample 2

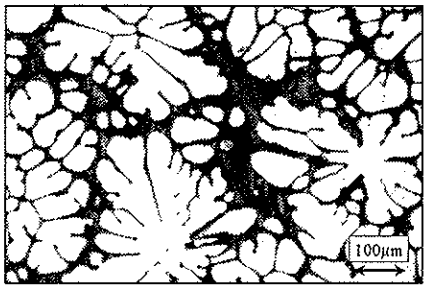


(c) Sample 3A

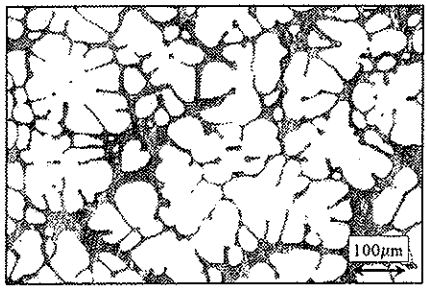


(d) Sample 3B

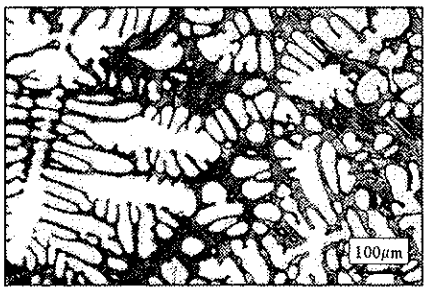


(e) Sample 4A

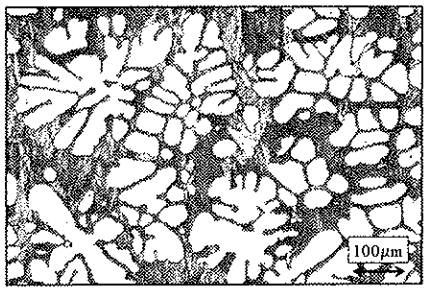


(f) Sample 4B

Figure 3: *Representative examples of the microstructures of the samples quenched from the mushy state. The light primary Al phase corresponds to the solid phase at the time of quenching.*

Table 2: *The experimental results from the morphology measurements* (Exp) *along with calculations using spherical grain envelopes, the hemispherical tip model, and FDM diffusion* (Mod). *The symbols are defined in the text and in the Nomenclature.*

| Sample | Source | $g_s^E$ | $S_s^E[10^4\mathrm{m}^{-1}]$ | $g_c^E$ | $S_e^E[10^4\mathrm{m}^{-1}]$ | $g_i^E$ |
|---|---|---|---|---|---|---|
| 1 | Exp | 0.906±0.003 | 4.5±0.1 | 0.953±0.003 | 2.1±0.1 | 0.951±0.004 |
| 4.70 wt.% Cu | Mod | 0.89 | 2.1 | 0.89 | 2.1 | 1.0 |
| 2 | Exp | 0.791±0.006 | 5.82±0.05 | 0.871±0.006 | 3.11±0.06 | 0.908±0.009 |
| 10.0 wt.% Cu | Mod | 0.75 | 2.1 | 0.75 | 2.1 | 1.0 |
| 3A | Exp | 0.644±0.005 | 6.94±0.07 | 0.819±0.007 | 2.8±0.2 | 0.786±0.009 |
| 14.9 wt.% Cu | Mod | 0.61 | 2.1 | 0.63 | 1.4 | 0.96 |
| 3B | Exp | 0.647±0.005 | 6.14±0.03 | 0.788±0.005 | 3.19±0.07 | 0.821±0.007 |
| 15.6 wt.% Cu | Mod | 0.59 | 2.1 | 0.59 | 2.1 | 1.0 |
| 4A | Exp | 0.499±0.004 | 7.26±0.09 | 0.81±0.01 | 2.0±0.2 | 0.61±0.01 |
| 20.1 wt.% Cu | Mod | 0.44 | 3.9 | 0.69 | 1.0 | 0.64 |
| 4B | Exp | 0.49±0.01 | 6.4±0.1 | 0.706±0.009 | 2.93±0.04 | 0.69 ±0.01 |
| 19.7 wt.% Cu | Mod | 0.46 | 4.4 | 0.52 | 1.5 | 0.89 |

grain envelopes. However, preferred growth directions and differences between primary and secondary arms typical for dendritic growth, are not discernible from these images. Although rarely mentioned in the literature, this type of equiaxed morphology ('clover-leaf') is very often observed in the as-cast microstructure of well grain refined Al alloys. Samples 3A and 4B (Figure 3c and f) are less globular and sets of arms or 'cells' aligned parallel to each other can be observed in addition to the 'clover-leaf' equiaxed patterns. In fact, at least in these limiting cases, the growth mode can not be determined from two-dimensional images alone. Sample 4A is the only sample which has a clear dendritic growth pattern in which primary and secondary dendrite arms can easily be distinguished from each other in a two-dimensional image.

# 4 The model

The model used to calculate the development of the microstructural morphology in the experiments was developed for the purpose of assessing the effect of the motion of the crystals on their evolution. Because the model is described in detail elsewhere [9,10], it is only briefly summarised here along with some additional simplifications and assumptions made in the present study. It is assumed that:

- there is no convection in the liquid phase and no crystal motion;
- the mass densities of the liquid and solid phases are equal;
- the specific heat capacities of the liquid and solid phases are equal;

Table 3: *Input parameters used in the equiaxed growth model*

| Quantity | Symbol | Value | Unit | Reference |
|---|---|---|---|---|
| Gibbs-Thompson constant | $\Gamma$ | $2.4\times10^{-7}$ | mK | [21] |
| Diffusivity of the liquid | $D_l$ | $3\times10^{-9}$ | $m^2/s$ | [21] |
| Diffusivity of the solid | $D_s$ | $3\times10^{-13}$ | $m^2/s$ | [21] |
| Specific latent heat | $L$ | $3.97\times10^{5}$ | J/kg | [21] |
| Specific heat capacity | $c_p$ | $1\times10^{3}$ | J/(kgK) | |

- the material properties are constant (the thermophysical data used in the calculations are given in Table 3);
- the nucleation occurs at the single instant when the temperature reaches the liquidus temperature of the alloy;
- the solidification of the primary Al phase ends at the instant when the eutectic temperature is reached.

The model is based on the models presented by Rappaz and Thévoz [5,6] and Wang and Beckermann [22], and relies upon three main ideas:

1. It is assumed that the crystals contained in a volume where variations in the temperature are negligible can be represented by a single unit sphere. The unit sphere contains one representative crystal having an average behaviour. The volume fractions of the different phases are defined relative to the total volume of this unit sphere. Furthermore, if the grains are assumed not to move relative to the solidifying sample, the diameter of the unit sphere can be set equal to the local final grain diameter, which can be related to the local grain density (Eq. (2)).
2. A virtual envelope is defined which connects the outermost points of the crystal in such a way that the envelope surface is minimised. The volume fraction of solid within the envelope, $g_i$, provides information about the global morphology: when $g_i < 1$ the crystal is porous (dendritic or 'clover-leaf'); when $g_i = 1$ the crystal is compact (globular). Thus, the change in morphology can be assessed without tracking the real complex solid/liquid interface.
3. In the model, the crystal evolution is controlled by the kinetics of the envelope and by solidification of the intragranular liquid phase (i.e., the liquid inside the envelope). These two driving phenomena are assumed to be independent of each other. Hence, during growth, the morphology results from the competition between the growth of the envelope and the solidification inside the envelope.

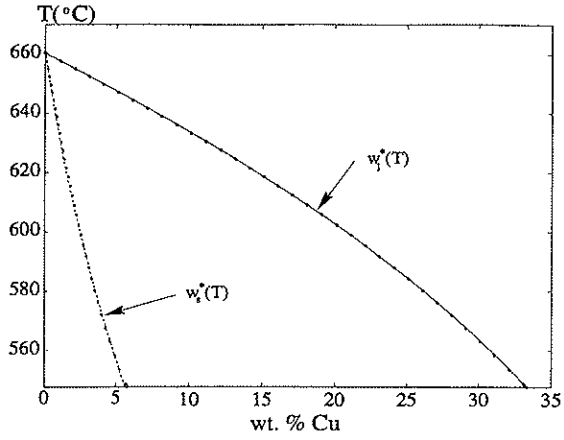


Figure 4: *The Al-Cu binary phase diagram [23].*

## 4.1 Mathematical formulation

The solidifying sample was assumed to have a uniform temperature. This is reasonable because the Biot number of the sample is in the order of $10^{-2} \ll 1$. This has two consequences: (*i*) a single unit sphere can be assumed to represent the whole sample; (*ii*) the temperature, $T$, can be related to the fraction of solid through the energy balance of the unit sphere, i.e.

$$\dot{Q} = c_p \frac{dT}{dt} - L \frac{dg_s}{dt} \tag{4}$$

where $\dot{Q}$ is the heat extraction rate and $t$ is the time.

Due to the low titanium and impurity contents (Table 1), the samples were treated as binary Al-Cu alloys in the calculations. We have assumed local thermodynamical equilibrium and negligible curvature effects at the solid/liquid interface. Hence, the solute concentration at the interface both in the solid, $w_s^*$, and in the liquid, $w_l^*$, was related to the temperature through the Al-Cu phase diagram as explained in Appendix A. The phase diagram was obtained from the ThermoCalc database [23] and is given in Figure 4.

For the sake of simplicity, the grain envelope was assumed to be either a sphere or an octahedron. Furthermore, the envelope shape was assumed to be preserved during the grain growth. For dendritic growth, this relates the velocities of the secondary dendritical instabilities to those of the primary dendrite tips in a simple manner. The envelope/liquid interfacial area concentration is given directly in terms of the grain density and the grain fraction:

$$S_e = \frac{1}{\phi_e} (36\pi n)^{1/3} g_e^{2/3} \tag{5}$$

where $\phi_e$ is the average shape factor or sphericity of the grain envelope defined as the

surface area of a sphere with the same volume as the envelope divided by the actual surface area of the envelope [1]. For a spherical envelope, $\phi_e = 1$ and for an octahedral one, $\phi_e = 0.85$ [9,10].

The envelope growth rate was assessed in two different ways depending on the value of the internal solid fraction: (*i*) for $g_i < 1$:

$$\frac{dg_e}{dt} = S_e V_m \tag{6}$$

where $V_m$ is the average normal velocity of the envelope; (*ii*) for $g_i = 1$:

$$\frac{dg_e}{dt} = \max\left(S_e V_m, \frac{dg_s}{dt}\right) \tag{7}$$

In the case of a spherical envelope, $V_m$ equals the velocity of a free dendrite tip, $V_t$. In the case of an octahedral envelope, $V_m = V_t/\sqrt{3}$. The velocity of the free dendrite tips, $V_t$, was assessed from dendrite tip growth models. These models are composed of two ingredients: (*i*) the solution of the solute diffusion equation around a tip with a given shape (paraboloidal or hemispherical [21]), and (*ii*) the marginal stability criterion proposed by Langer *et al.* [24].

The solidification inside the envelope was described by solute balances at the scale of the grain. In the solid phase:

$$\frac{d}{dt}(g_s w_s) = S_s J_s + w_s^* \frac{dg_s}{dt} \tag{8}$$

where $w_s$ is the average solute concentration in the solid phase, and $J_s$ is the diffusive solute flux across the solid/liquid interface into the solid phase. In the intragranular liquid, a complete solute mixing was assumed: the solute concentration in the intragranular liquid is then equal to the concentration of the liquid phase at the solid/liquid interface. The solute balance becomes:

$$w_l^*(1-k)\frac{dg_s}{dt} = -S_s J_s - S_e J_l + (g_e - g_s)\frac{dw_l^*}{dt} \tag{9}$$

where $J_l$ is the diffusive solute flux across the envelope into the extragranular liquid (outside the envelope). In the extragranular liquid:

$$\frac{d}{dt}[(1-g_e)w_l] = S_e J_l - w_l^* \frac{dg_e}{dt} \tag{10}$$

where $w_l$ is the average solute concentration in the extragranular liquid.

The diffusive solute flux across the solid/liquid interface into the solid phase, $J_s$, was found by a collocation method in which $J_s$ is related to $w_s^*$, $w_s$ and to a characteristic length of the solid microstructure (see Refs. [9,10] for more details). The diffusive solute flux across the envelope into the extragranular liquid, $J_l$, was found by one of the following two methods: (*i*) A boundary layer approach where $J_l$ can be expressed as:

$$J_l = D_l \frac{w_l^* - w_l}{\delta} \tag{11}$$

where $D_l$ the solute diffusivity in the liquid. The boundary layer thickness, $\delta$, was set equal to the ratio between $D_l$ and $V_m$ (this method is called D/V diffusion in the present paper). (*ii*) A solution of the solute diffusion equation in the extragranular liquid assuming spherical symmetry and using a finite difference scheme and a Landau transformation (see Refs. [10,25]) (this method is called FDM diffusion in the present paper).

In order to solve the set of equations, the solid/liquid interfacial area concentration, $S_s$, must be specified. Appolaire *et al.* [9] suggested a relation for $S_s$ which can be written in terms of the morphological quantities defined in Section 2.2:

$$S_s = \frac{4}{\lambda_2} g_i^{1/2} g_e (1 - g_i^p) + g_i^p S_e \tag{12}$$

where $p$ is a parameter and $\lambda_2$ is the secondary dendrite arm spacing calculated from the expression proposed by Mortensen [26]. For low values of $g_i$, the last term on the right-hand side of Eq. (12) is negligible and $S_s \simeq 4 g_i^{1/2} g_e / \lambda_2$, which can be deduced by assuming a dendritic structure with cylindrical secondary arms [9, 10]. For values of $g_i$ close to 1, the first term on the right-hand side of Eq. (12) is negligible and $S_s$ tends towards $S_e$.

## 4.2 Solution procedure

In addition to the material properties (Table 3), the input parameters of the model are:

- The grain density which was set equal to the experimental value (Table 1) obtained as described in Section 2.2.
- The heat extraction rate which was assumed to be a constant given for each sample by the values in Table 1 (deduced from the experimental temperature-time curves). The validity of assuming a constant heat extraction rate in the calculations is discussed in Appendix B.
- The exponent $p$ which appears in Eq. (12). In order to estimate the value of this exponent, it was calculated for each sample by inserting the measured morphology parameters in Eq. (12) and solving for $p$. The resulting values are shown in Table 4. The mean value $p = 6$ was used in all the calculations; Table 5 reveals the error induced by this simplification. It should be emphasised that Eq. (12) probably represents a quite crude estimate of $S_s$ which was used due to lack of experimentally validated relations.

For the full details of the solution procedure, the reader is referred to Reference [10]. The procedures involved in the use of the phase diagram data from ThermoCalc [23] are, furthermore, described in Appendix A. In particular, this concerns the use of a liquidus slope and a partition coefficient which vary with the temperature. The calculation time

Table 4: *The value of the exponent p in Eq. (12) calculated from the measured morphology parameters for each experimental case.*

| Sample | 1 | 2 | 3A | 3B | 4A | 4B | Mean |
|---|---|---|---|---|---|---|---|
| $p$ | – | 8.8 | 4.5 | 6.5 | 2.4 | 7.8 | 6.0 |

Table 5: *Comparison between the solid/liquid interfacial area concentration, $S_s$, obtained experimentally* (Exp) *and calculated by Eq (12) using $p = 6$ and the experimental values of the other morphological quantities. All values are reported in* $10^4$ $m^{-1}$.

| Sample | 1 | 2 | 3A | 3B | 4A | 4B |
|---|---|---|---|---|---|---|
| $S_s$ Exp | 4.5 | 5.82 | 6.94 | 6.14 | 7.26 | 6.4 |
| $S_s$ Eq (12) | – | 5.2 | 7.6 | 6.0 | 9.3 | 6.2 |

step was set to $10^{-2}$ s in order to prevent numerical divergence. 500 nodes was used in the extragranular liquid in order to obtain sufficient accuracy in the calculation of the diffusive solute flux at the envelope (FDM diffusion).

# 5 Comparison between modelling predictions and the measured morphology

With the growth model described in Section 4, different results are obtained dependent on the choice of the main model assumptions: the grain envelope shape, the model for the solute diffusion in the extragranular liquid, and the model for the dendrite tip growth. In this Section, the effect of changing these model assumptions in a typical case (Sample 3A) is discussed. Furthermore, modelling predictions for the different experimental conditions discussed previously are presented along with possible explanations for discrepancies between the predictions and the measurements.

## 5.1 The effect of the envelope shape

In order to estimate the grain density from the linear intercept measurements, as shown in Section 2.2, it is necessary to assume an envelope shape. Therefore, a calculation of the envelope shape factor, $\phi_e^E$, using Eq. (5) based on the measured values of $S_e^E$, $n^E$, and $g_e^E$, would be spurious. A rough estimate of $\phi_e^E$ can, however, be obtained from the two-dimensional images using the procedure suggested in Reference [2]. With this procedure, the value of $\phi_e^E$ was estimated to be between 0.78 and 0.82 for the samples in this study.

A spherical envelope shape minimises the surface to volume ratio of the grains. Because the true value of $\phi_e$ is less than 1, the assumption of spherical envelopes will under-

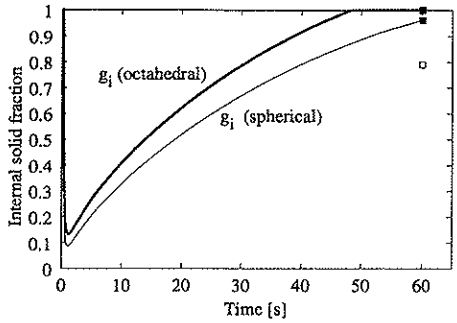


Figure 5: *The effect of the envelope shape on the development of the internal solid fraction, $g_i$ (Sample 3A, hemispherical tip model, and FDM diffusion). The open square represents the experimental value and the closed squares represent the end points of the calculated curves.*

estimate the measured values of $S_e^E$. An envelope shape with a lower shape factor (e.g., the octahedral shape) would decrease this discrepancy. However, such a choice would increase the value of $S_e$ throughout the calculation, and thereby increase the solute flux at the envelope. In turn, this would result in lower undercoolings and more globular morphologies than observed experimentally. This effect is revealed in Figure 5, where it is shown that a spherical envelope shape gives the best prediction of the internal solid fraction. It should be noted that a spherical envelope shape is consistent with the assumption of spherical symmetry in the estimation of the grain densities from the linear intercept measurements as well as in the solution of the diffusion equation in the extragranular liquid.

## 5.2 The effect of the tip model

It is generally accepted that the shape of a freely growing primary dendrite tip is well approximated by a paraboloid of revolution. For the morphologies observed in this study, however, it turns out that choosing a hemispherical shape gives a better agreement between the modelled and the experimental results. Figure 6 reveals the differences in the development of the internal solid fraction, $g_i$, using hemispherical and paraboloidal tip models. The higher tip velocity associated with a hemispherical tip increases the envelope growth rate during recalescence. Thus, the minimum in the $g_i(t)$ curve occurs at a lower value of $g_i$ using the hemispherical tip model than using the paraboloidal tip model. Using the hemispherical tip model, the solidification in the intragranular region does not complete ($g_i^E < 1$) before the eutectic temperature is reached. However, the modelling prediction of $g_i^E = 0.96$ corresponds to a more globular morphology than the measured one ($g_i^E = 0.786$, Figure 3(c)). With a paraboloidal tip model, the modeled morphology

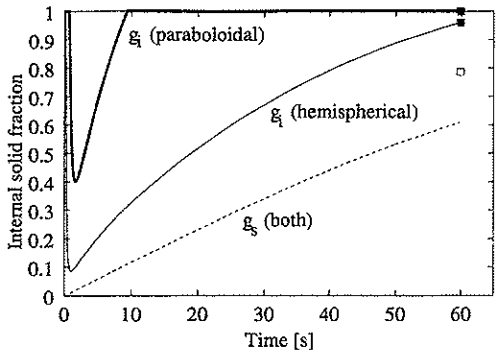


Figure 6: *The effect of the tip model on the development of the internal solid fraction, $g_i$ (Sample 3A, spherical envelopes, and FDM diffusion). The open square represents the experimental value and the closed squares represent the end points of the calculated curves. With a paraboloidal shape, the modeled morphology becomes globular already at a solid fraction $g_s \simeq 0.1$ for Sample 3A, which does not comply with the experimentally observed morphology (Figure 3(c)).*

becomes globular already at $g_s \simeq 0.1$ for the case in Figure 6.

Physically, it is not clear why the best agreement is achieved using the hemispherical tip model. However, a visual inspection of the images in Figure 3 indicates that many of the tips appear more like hemispherical needles than like paraboloids. For the dendritic Sample 4A (Figure 3(e)), this tendency is less clear. As opposed to the other samples, choosing the paraboloidal tip model for Sample 4A does not result in a completely globular modelled morphology. However, even for this dendritic sample, using the hemispherical tip model gives predictions that are closer to the experimental results than predictions obtained by using the paraboloidal tip model. Anyway, the choice of the tip model is revealed to have a large effect on the modelled morphology development.

## 5.3 The effect of solute diffusion in the extragranular liquid

During the course of solidification, diffusion of solute from the intragranular to the extragranular liquid acts to reduce the constitutional undercooling. The tip growth and thereby the envelope growth rate is very sensitive to this undercooling. As a result, the modelled morphology becomes sensitive to the way the diffusion in the extragranular liquid is modelled.

It has, however, been pointed out in Reference [8] that the prediction of the cooling curve by the type of equiaxed growth model used in the present study is relatively insensitive to the choice of the diffusion length in the extragranular liquid at the envelope. For this reason, it is common in micro-macro modelling to introduce the simplification

that the diffusion length $\delta$ in Eq. (11) is equal to $D_l/V_m$. In this case, the solute balance in the extragranular liquid phase (Eq. (10)) becomes

$$(1 - g_e)\frac{dw_l}{dt} = 0 \tag{13}$$

where $w_l$ is the average solute concentration in the extragranular liquid. Eq. (13) shows that there will be no enrichment of the extragranular liquid (i.e., $dw_l/dt = 0$) as long as $g_e < 1$. Thus, with this diffusion length, there is no reduction of the undercooling due to diffusion, and the grains grow quickly to fill all available space (Figure 7). This result is not consistent with the situation in the experiments presented in this study, where a significant extragranular liquid fraction, $(1 - g_e)$, is observed in all the cases.

Solving the diffusion equation in the extragranular liquid at each time step is more time consuming, but with this procedure the growth model does not suffer from the shortcoming expressed by Eq. (13). In this case, diffusion causes a solute flux across the envelope surface, which in turn leads to a reduced undercooling and a decrease in the envelope growth rate, $dg_e/dt$, as shown in Figure 7. Physically, the reduced undercooling is caused by the gradual overlapping of the diffusion fields of neighbouring grains.

## 5.4 Modelling predictions for the different experimental conditions

The modelling results which give the best overall fit with the experimental results are obtained using spherical grain envelopes, the FDM solution of the diffusion equation in the extragranular liquid, and the hemispherical tip model. Modelling results are shown in Table 2.

The predicted solid fractions in this calculation are lower than the measured values for all samples, with a maximum discrepancy of about 0.05. A possible explanation for this discrepancy is the modelling assumption of equal solid and liquid densities introduced to avoid changes in unit sphere volume. This is seen by applying the lever rule and the solid and liquid densities suggested by Ganesan and Poirier [27] to calculate the mass and volume fraction of solid for the alloys in this study. The resulting discrepancies between the mass and volume fractions are then in the same direction and of the same order of magnitude as the discrepancies between the measured volume fractions of solid and the calculated solid fractions in Table 2.

The prediction of the solid/liquid interfacial area concentration, $S_s$, is determined by the values of the other morphological parameters along with the exponent $p$ (Eq. (12)). For Sample 1, 2, and 3B, globular grains are predicted ($g_i^E = 1$) and thus $S_s^E = S_e^E$ (Table 2). It should be emphasised that a small deviation from globularity (e.g., $g_i^E \simeq 0.95$) gives a large deviation in $S_s^E$ because even very narrow spaces between the 'cells' or secondary dendrite arms are associated with quite considerable interfacial area. Con-

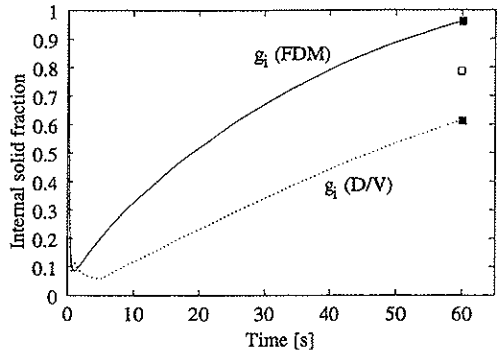


(a) *Internal solid fraction*

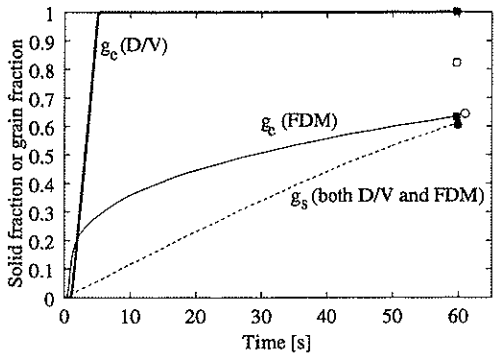


(b) *Solid fraction and grain fraction*

Figure 7: *The effect of two different ways of modelling the solute diffusion in the extra-granular liquid on (a) the internal solid fraction and (b) the solid fraction and the grain fraction. With a diffusion length equal to $D_l/V_m$ (D/V), the envelope grows quickly to fill all available space ($g_e = 1 \Rightarrow g_i = g_s$). With a solution of the diffusion equation outside of the grain (FDM), the envelope growth slows down due to overlapping of the diffusion fields of neighbouring grains. The open symbols represent the experimental values and the closed squares represent the end points of the calculated curves.*

sequently, the prediction of $S_s^E$ is very sensitive to the prediction of $g_i^E$. However, even in a case where the modelling prediction of $g_i^E$ is good (e.g., Sample 4A), the calculated value of $S_s^E$ can be considerably lower than the measured one. This is partly due to the fact that the value of $S_e^E$ is underestimated. In addition, the use of an average value of the exponent $p$ in Eq. (12) can increase the discrepancy because the value of the exponent varies from $p = 2.4$ for Sample 4A to $p = 8.8$ for Sample 2 (Table 4). In a typical modelling case, the value of $S_s^E$ changes by a factor of 2 when the value of $p$ is changed from 2.4 to 8.8. It should be noted that changing the value of $p$ in the model does not affect the other morphology parameters.

As shown in Table 2, the modelling predictions of the internal solid fraction, $g_i^E$, overestimate the measured values for all the experimental cases. For Sample 4A, which has a dendritic morphology, the discrepancy is small, but for all the other samples, the error is considerable. The too rapid globularisation ($dg_i/dt > 0$) is a result of the reduced envelope velocity as well as the continuing removal of solute by diffusion across the envelope into the extragranular liquid. The relation between the velocity of the envelope and the undercooling is based on the assumption that the tips grow independently of each other, in the sense that the diffusion fields ahead of each tip is not influenced by the diffusion fields ahead of the neighbouring tips. This assumption is hardly fulfilled after the start of the overlapping of the diffusion fields of neighbouring grains: at this stage, the tips grow to fill the extragranular spaces between the grains and the probability to interact with neighbouring tips is high. Moreover, the morphologies in Figure 3 (e.g., Sample 2 and Sample 3B), indicate that enriched liquid can be trapped inside the grain envelopes (i.e., the intragranular liquid is no longer well mixed). If this entrapment reduces the diffusion of solute across the envelope, the undercooling and thus the envelope growth rate would reduce more slowly which would prevent globularisation. More experimental results as well as modelling efforts are needed in order to improve the understanding of how the internal solid fraction develops during solidification of Al alloys.

The prediction of the envelope/liquid interfacial area concentration, $S_e$, relies on the prediction of $g_e$, the measured value of the grain density, and the choice of the envelope shape (Eq. (5)). Table 2 shows that the predicted values of $S_e^E$ are low compared with the measured values. This is due to the choice of a spherical envelope along with the underestimation of $g_e^E$, as discussed previously.

# 6 Prediction of the mushy zone permeability

In mathematical modelling of casting processes, the morphology dependent macroscopic mushy zone properties are calculated through constitutive relations. For example, in macroscopic fluid flow calculations, the mushy zone permeability can be calculated by the Kozeny-Carman relation or by the more elaborate model suggested by Wang & Beck-

Table 6: *Mushy zone permeability values for the measured* (Exp) *and for the predicted* (Mod) *morphology parameters in Table 2 calculated by the relation suggested by Wang & Beckermann [1]. All the values are reported in* [$m^2$].

| Sample | 1 | 2 | 3A | 3B | 4A | 4B |
|---|---|---|---|---|---|---|
| Exp | $7\times10^{-14}$ | $6\times10^{-13}$ | $2\times10^{-12}$ | $3\times10^{-12}$ | $7\times10^{-12}$ | $9\times10^{-12}$ |
| Mod | $7\times10^{-13}$ | $8\times10^{-12}$ | $6\times10^{-11}$ | $3\times10^{-11}$ | $8\times10^{-11}$ | $1\times10^{-10}$ |

ermann [1]. Even if these relations provide a good description of the permeability as a function of a set of morphology parameters, an error in the predicted morphology can induce a large uncertainty in the predicted permeability.

The accuracy of the mushy zone permeability predictions can be estimated from the magnitude of the discrepancy between the morphology measurements and the modelling predictions observed in the present study. The permeability for the measured and for the predicted morphology parameters in Table 2 was calculated by the relation suggested by Wang & Beckermann [1]. The results are presented in Table 6, where we can see that the predicted morphology parameters overestimate the permeability by a factor of 10 to 30 for the different samples. Consequently, in micro-macro modelling of casting processes involving the type of grain morphology observed in the present study, the relative error in the calculated permeability could be around one order of magnitude.

# Conclusions

For the purpose of testing the predictions of an equiaxed growth model recently presented elsewhere [9,10], the microstructural morphology of equiaxed Al-Cu alloys has been assessed at a single point during solidification by quenching solidifying samples at the instant when the eutectic temperature is reached. A recently developed metallographic method has been used to distinguish between the intragranular and extragranular length scales in the microstructure. For the equiaxed morphologies observed in the present study, the growth model [9,10] predicts higher values of the internal solid fraction than observed experimentally. This has been indicated to be due to the failure of commonly made modelling assumptions during the later stages of the solidification. The discrepancies has been shown to have a large effect on the calculation of the mushy zone permeability, which in turn can induce errors in micro-macro modelling. More experimental results as well as modelling efforts are needed in order to improve the understanding of how the internal solid fraction and the interfacial area concentrations develops during equiaxed solidification of Al alloys.

# Nomenclature

$A$ stereological constant
$c_p$ specific heat capacity, J/(kgK)
$d$ average centre-to-centre distance between grains, m
$D_l$ diffusivity in the liquid, $m^2/s$
$D_s$ diffusivity in the solid, $m^2/s$
$g_s$ volume fraction of the solid phase
$g_e$ volume fraction of the grain envelopes
$g_i$ volume fraction of solid within the grain envelopes
$h$ specific enthalpy, J/kg
$J_l$ diffusive solute flux across the envelope into the extragranular liquid phase
$J_s$ diffusive solute flux across the solid/liquid interface into the solid phase
$k$ partition coefficient
$\bar{l}$ mean linear intercept, m
$L$ specific latent heat, J/kg
$m$ slope of the liquidus line, °C/wt.%
$n$ grain density, grains/$m^3$
$p$ exponent in solid/liquid interfacial area concentration relation
$\dot{Q}$ heat extraction rate, J/kgs
$\dot{Q}_{exp}$ average experimental heat extraction rate, J/kgs
$S$ surface to volume ratio of sample, $m^{-1}$
$S_s$ solid/liquid interfacial area concentration, $m^{-1}$
$S_e$ envelope/liquid interfacial area concentration, $m^{-1}$
$t$ time, s
$t_{exp}$ measured solidification time, s
$T$ temperature, degrees Celsius
$T_{eut}$ eutectic temperature, degrees Celsius
$T_g$ temperature in the graphite crucible, degrees Celsius
$T_{liq}$ liquidus temperature, degrees Celsius
$V_m$ average normal velocity of the envelope, m/s
$V_t$ velocity of a free dendrite tip, m/s
$w_0$ nominal copper concentration in a sample, wt.%
$w_l$ average solute concentration in the extragranular liquid phase, wt.%
$w_l^*$ solute concentration in the liquid at the solid/liquid interface, wt.%
$w_s$ average solute concentration in the solid phase, wt.%
$w_s^*$ solute concentration in the solid phase at the solid/liquid interface, wt.%
$\alpha_{ga}$ heat transfer coefficient at graphite-air interface, J/(kgKs)
$\alpha_{mg}$ heat transfer coefficient at metal-graphite interface, J/(kgKs)

$\delta$ solute diffusion length at the envelope in the extragranular liquid phase, m
$\Delta t$ calculation time step, s
$\Gamma$ Gibbs-Thompson constant, mK
$\lambda_2$ cell or secondary dendrite arm spacing, $\mu$m
$\phi_e$ shape factor of the grain envelopes

## Acknowledgements

The authors want to thank Mrs. G. Berg, SINTEF, for performing the delicate sample preparation required for the morphology characterisation. Thanks are also due to Ms. I. Furulund, SINTEF, for help with the optical microscopy, and to Mr. I. Farup for assistance with the heat transfer modelling in Appendix B. We are also grateful to Prof. G. Lesoult and Prof. L. Arnberg for valuable discussion and suggestions.

The present work was funded by the Brite-EuRam project EMPACT with Project No.BE-1112 and Contract No.BRPR-CT95-0112, and with the following partners: Hoogovens Corporate Services BV (The Netherlands); Hydro Aluminium AS (Norway); Elkem Aluminium ANS (Norway); Pechiney Recherche (France); Vereinigte Aluminiumwerke AG (Germany); Alusuisse-Lonza Services AG (Switzerland); Calcom SA (Switzerland); Technische Universiteit Delft (The Netherlands); Institut National Polytechnique de Lorraine (France); and Ecole Polytechnique Federale de Lausanne (Switzerland). SINTEF together with the Norwegian University of Science and Technology participate in the EMPACT Project as a major sub-contractor to Hydro Aluminium AS and Elkem Aluminium ANS. The authors thank the EMPACT partners and the European Commission for financial support.

## Appendix A: Accommodation procedure for the phase diagram data

In the present study, the liquidus curve was expressed as:

$$T = a_1 w_l^{*2} + a_2 w_l^* + a_3 \tag{A14}$$

where $w_l^*$ is the solute mass fraction of the liquid phase at thermodynamic equilibrium, and the coefficients $a_i$, $i = 1..3$, given in Table 7, are based on a polynomial fit performed on coordinates for the liquidus curve of the Al-Cu diagram obtained from the ThermoCalc database [23] (Figure 4).

In a similar way, a linear expression for the partition coefficient has been determined from a linear least squares regression on partition coefficients obtained from the phase

Table 7: *Thermodynamical data used in the equiaxed growth model.*

| Quantity | Symbol | Value | Unit | Reference |
|---|---|---|---|---|
| Eutectic temperature | $T_{eut}$ | 547.7 | °C | [23] |
| Coefficients in Eq. (A14) | $a_1$ | -0.0343726 | °C/(wt.%)$^2$ | [23] |
| | $a_2$ | -2.16885 | °C/wt.% | [23] |
| | $a_3$ | 659.4 | °C | [23] |
| Coefficients in Eq. (A17) | $b_1$ | $1.4\times10^{-3}$ | 1/wt.% | [23] |
| | $b_2$ | $9.45\times10^{-2}$ | | [23] |

diagram [23]:

$$k = b_1 w_l^* + b_2 \tag{A15}$$

In order to keep the solution procedure of the model which handles constant liquidus slope, $m$, and partition coefficient, $k$, we have supposed that $m$ and $k$ were constant during a calculation time step, $\Delta t$, and equal to their values at the previous time step:

$$m(t) = \left(\frac{\partial T}{\partial w_l^*}\right)_t = 2a_1 w_l^*(t) + a_2 \tag{A16}$$

$$k(t) = \frac{w_s^*(t)}{w_l^*(t)} = b_1 w_l^*(t) + b_2 \tag{A17}$$

where $w_s^*$ is the solute mass fraction of the solid phase at thermodynamic equilibrium. Hence, the sample temperature, $T$, at the new time step, $t + \Delta t$, was written as:

$$T(t + \Delta t) = T(t) + m(t)[w_l^*(t + \Delta t) - w_l^*(t)] \tag{A18}$$

At the end of a new time step, $w_l^*(t + \Delta t)$ is known, and the $m$ and $k$ can be updated by Eqs. (A16–A17).

# Appendix B: The heat flow in the experiment

In the modelling of the heat flow in the type of experiment performed in this study, it is often assumed that the heat extraction rate, $\dot{Q}$, is a constant which can be estimated e.g., from the cooling rate, $\dot{T}$, prior to the start of solidification by $\dot{Q} = c_p \dot{T}$. However, in the present work, the measured solidification times lead to average values of $\dot{Q}$ (cf. Eq. (3)), that are about a factor of two *higher* than the values obtained from the cooling rate prior to solidification. This means that $\dot{Q}$ increases during solidification, and it was decided to use the constant average heat extraction rates obtained from Eq. (3) in the calculations.

In order to check whether or not the assumption of a constant heat extraction rate is reasonable, a varying $\dot{Q}$ with time during solidification was studied in a simple heat

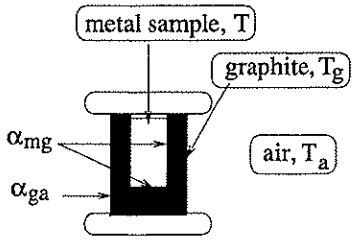


(a) The model problem

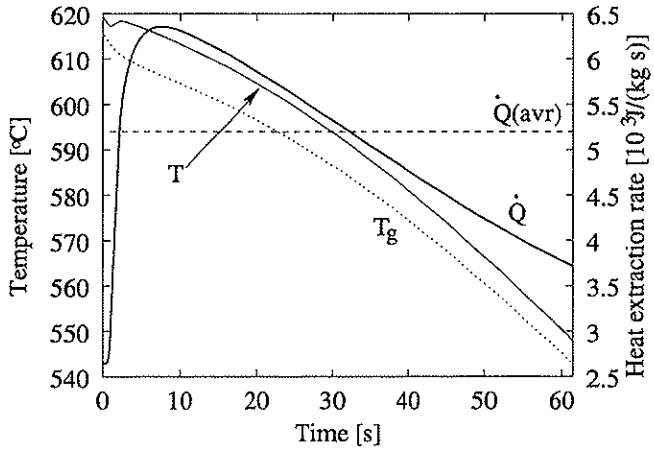


(b) A typical modelling result

Figure 8: *Results from a heat flow model of the solidification experiment. The temperature in the metal sample, $T$, and in the graphite mould, $T_g$, was assumed to be uniform while the surrounding air remains at room temperature, $T_a$. $\dot{Q}$ and $\dot{Q}(avr)$ denote the time dependent heat extraction rate calculated by Eq. (B19) and the average heat extraction calculated by Eq. (3), respectively. $\alpha_{mg}$ and $\alpha_{ga}$ denote the heat transfer coefficients at the metal-graphite and graphite-air interfaces, respectively.*

flow model. It was assumed that the metal sample and the graphite mould each has a uniform temperature and that the surrounding air remains at room temperature during the experiment. Furthermore, the heat transfer at the two interfaces (metal-graphite and graphite-air) was modelled by two constant heat transfer coefficients. The solidification path was given by the enthalpy as a function of the solid fraction, $h = c_p T + L(1 - g_s)$. This path was calculated by the growth model using a constant value of $\dot{Q}$. Thus, the temperature in the sample, $T$, and in the mould, $T_g$, were calculated as functions of time, along with the heat extraction rate given by:

$$\dot{Q}(t) = S\alpha_{mg}(T(t) - T_g(t)) \tag{B19}$$

where $S$ is the surface to volume ratio of the sample and $\alpha_{mg}$ is the heat transfer coefficient between the sample and the graphite mould.

As shown in Figure 8, the evolution of latent heat right after the start of the solidification reduces the cooling rate of the sample ($dT/dt$) more than it reduces the cooling rate of the mould ($dT_g/dt$). Thereby, the temperature difference ($T - T_g$) between the sample and the mould increases, which causes an increased $\dot{Q}$ from the sample due to Eq. (B19). The calculated $\dot{Q}(t)$ curve was implemented in the equiaxed growth model by evaluating the value of $\dot{Q}(t)$ at each time step. Figure 9 shows the temperature and the development of the internal solid fraction in modelling cases with constant and varying $\dot{Q}$. With a varying $\dot{Q}$, recalescence occurs at a lower undercooling because the instantaneous $\dot{Q}$ is lower than the average value in this region. However, during recalescence, the instantaneous $\dot{Q}$ increases above the average value and the undercooling becomes higher for the case with a varying $\dot{Q}$. As shown in Figure 9, these two counteracting effects result in a development of the morphology which is not significantly different in the two cases. This was found to be true for all the samples, which indicates that even if the assumption of a constant heat extraction rate is not strictly correct, the use of this assumption in the present context does not influence the predicted results significantly.

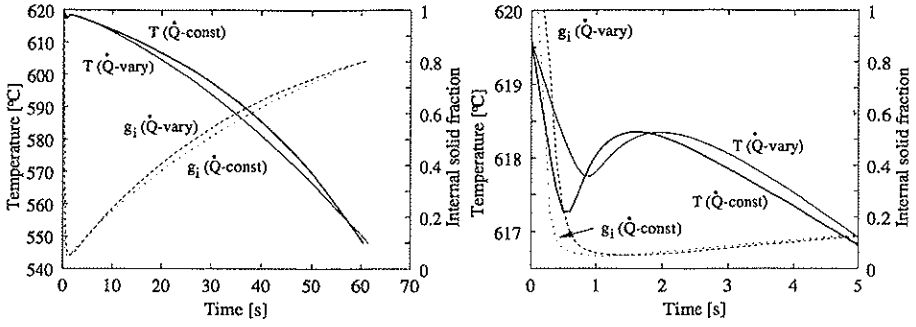


Figure 9: *The effect of a varying and constant heat extraction rate, $\dot{Q}$, on the predicted temperature, $T$, and on the development of the internal solid fraction, $g_i$. (b) is a close-up of (a) in the first 5 seconds.*

# References


[1] C. Y. Wang, S. Ahuja, C. Beckermann, and H. C. de Groh III. Multiparticle interfacial drag in equiaxed solidification. *Metallurgical Transactions B*, **26B**:111–19, 1995.

[2] Ø. Nielsen, L. Arnberg, A. Mo, and H. Thevik. Experimental determination of the mushy zone permeability in Al-Cu alloys with equiaxed microstructures. *Metallurgical and Materials Transactions A*, **30A**:2455–62, 1999.

[3] M. Rappaz Ph. Thevoz, J. L. Desbiolles. Modeling of equiaxed microstructure formation in casting. *Metallurgical Transactions A*, **20A**:311–322, 1989.

[4] C. Y. Wang and C. Beckermann. Equiaxed dendrite solidification with convection: Part II. numerical simulations for an Al-4 wt.% Cu alloy. *Metallurgical and Materials Transactions A*, **27A**:2765–83, 1996.

[5] M. Rappaz and Ph. Thévoz. Solute diffusion model for equiaxed dendritic growth. *Acta Metallurgica*, **35**:1487–97, 1987.

[6] M. Rappaz and Ph. Thévoz. Solute diffusion model for equiaxed dendritic growth: Analytical solution. *Acta Metallurgica*, **35**:2929–33, 1987.

[7] C. Y. Wang and C. Beckermann. A unified solute diffusion model for columnar and equiaxed dendrite alloy solidification. *Materials Science and Engineering*, **A171**:199–211, 1993.

[8] C. Y. Wang and C. Beckermann. A multiphase solute diffusion model for dendritic alloy solidification. *Metallurgical Transactions A*, **24A**:2787–2802, 1993.

[9] B. Appolaire, H. Combeau, and G. Lesoult. Modelling of equiaxed crystal evolution in the presence of convection for multicomponent alloys. *Submitted to Journal of Crystal Growth*, 1999.

[10] B. Appolaire. *Prise en compte du mouvement des cristaux équiaxes dans la modélisation de la solidification des lingots d'acier coules en fonderie.* PhD thesis, Institut National Polytechnique de Lorraine, France, 1999.

[11] L. Bäckerud and M. Johnsson. The relative importance of nucleation and growth mechanisms to control grain size in various aluminum alloys. In W. Hale, editor, *Light Metals 1996*, pages 679–685, 1996.

[12] A. M. Figuerdo, Y. Sumartha, and M. C. Flemings. Measurement and calculation of solid fraction in quenched semi-solid melts of rheocast aluminium alloy A357. In *Light Metals 1998*, pages 1103–1106, 1998.

[13] S. W. Chen and C. C. Huang. Solidification curves of Al-Cu, Al-Mg and Al-Cu-Mg alloys. *Acta Materialia*, **44**:1955–65, 1996.

[14] L. Arnberg, L. Bäckerud, and G. Chai. *Solidification characteristics of aluminum alloys*, volume vol. 3: Dendritic coherency. AFS, Inc., 1996.

[15] D. R. Poirer and S. Ganesan. Permeabilities for flow of interdendritic liquid in equiaxial structures. *Materials Science and Engineering*, **A157**:113–23, 1992.

[16] D. R. Poirer and P. Ocansey. Permeability for flow of liquid through equiaxial mushy zones. *Materials Science and Engineering*, **A171**:231–40, 1993.

[17] S. Viswanathan, A. J. Duncan, A. S. Sabau, and Q. Han. Prediction of microporosity in aluminium. In B. G. Thomas and C. Beckermann, editors, *Modeling of casting, welding and advanced solidification processes VIII*, pages 849–856. TMS, Warrendale, PA, 1998.

[18] T. Magnusson, Ø. Nielsen, L. Pedersen, and P. A. Tøndel. A comparison between to temperature measuring systems. Technical report STF24 A98541, SINTEF, 1998.

[19] A. W. Thompson. Calculation of true volume grain diameter. *Metallography*, **5**:366–69, 1972.

[20] R. L. Fullman. Measurement of particle sizes in opaque bodies. *Transactions of the Metallurgical Society of AIME*, **197**:447–52, 1953.

[21] W. Kurz and D. J. Fisher. *Fundamentals of solidification.* Trans Tech Publications, 1992. page 294.

[22] C. Y. Wang and C. Beckermann. Equiaxed dendrite solidification with convection: Part I. multiscale/multiphase modeling. *Metallurgical and Materials Transactions A*, **27A**:2754–64, 1996.

[23] I. Ansara, A. T. Dinsdale, and M. H. Rand, editors. *EUR18171-COST507 Thermochemical database for light metall alloys*, volume 2. Office for the Official Publications of the European Communities, Luxenbourg, 1998-XI.

[24] J. S. Langer and H. Müller-Krumbhaar. *Acta Metallurgica*, **26**:1681; 1689; 1697, 1978.

[25] M. Rappaz and W. J. Boettinger. On dendritic solidification of multicomponent alloys with unequal liquid diffusion coefficients. *Acta Materialia*, **47**:3205–19, 1999.

[26] A. Mortensen. On the rate of dendrite arm coarsening. *Metallurgical Transactions A*, **22A**:569–574, 1991.

[27] S. Ganesan and D. R. Poirier. Densities of aluminum-rich aluminum-copper alloys during solidification. *Metallurgical Transactions A*, **18A**:721–23, 1987.

# Concluding remarks and future challenges

This thesis has addressed the assessment of the mushy zone permeability in equiaxed aluminium alloys. The approach taken has been to experimentally determine the permeability of binary Al-Cu alloys as a function of a set of parameters describing the microstructural morphology. Moreover, the morphology parameters have been experimentally determined during solidification of binary Al-Cu alloys in order to evaluate the morphology predicted by an equiaxed growth model commonly used in micro-macro modelling.

An important outcome of the thesis work is the development of the experimental method and apparatus for permeability measurements presented in Article 1 and Article 2. In particular, the electron-beam welding of the flux alloy and sample prior to remelting in the permeameter was an important break-through that contributed to the reproducibility of the experiment and to the high accuracy in the measured permeability compared with previous works. Furthermore, the method developed for the quantification of the grain morphology of the samples on multiple length scales increases the value of the permeability measurements because the measurements can now be compared with the most recent permeability models available in the literature.

The permeability measurements presented in this thesis indicate that both the Kozeny-Carman relation and the more recent model used in Article 1 provide good descriptions of the permeability of the mushy zone. For the experimental cases in Article 1, the models apply even at solid fractions as high as 0.91. The validation of these permeability models is an important progress because models that predict the formation of casting defects are often very sensitive to the permeability.

At present, permeability measurements for aluminium alloys with a corresponding morphology characterisation have been restricted to Al-Cu alloys, eutectic composition of the interdendritic liquid, and remelting of the sample. In order to check the assumption that the permeability depends solely on the solid fraction along with parameters describing the grain morphology, measurements should be performed on other aluminium alloys. For example, the experimental method presented in Article 1 could be used to measure the permeability of a mushy zone with a morphology formed during eutectic solidification. Moreover, in order to validate the permeability models for relevant solidification conditions, the permeability should be measured during solidification rather than during remelting. The experimental difficulties associated with these future challenges have been found to be considerable, as discussed in Article 2. These challenges could be met by a further development of the permeameter used in this thesis, as well as by completely new concepts for permeability measurements.

As reported in the literature, problems were encountered when trying to quantify the grain morphology during solidification by quenching experiments. Therefore, the measurements reported in Article 3 were restricted to the instant when the interdendritic liquid reaches the eutectic composition. In spite of this limitation, it should be noted that measurements of morphology parameters at two length scales have not been reported earlier for equiaxed aluminium alloys. The comparison between the equiaxed growth model and the measurements shows that the model predicts higher values of the internal solid fraction (i.e., a more globular morphology) than observed experimentally. This has been indicated to be due to the failure of commonly made modelling assumptions during the later stages of the solidification. More experimental results as well as modelling efforts are needed in order to improve the understanding of how the internal solid fraction and the interfacial area concentrations develops during equiaxed solidification of aluminium alloys. In addition, the physical mechanisms responsible for the development of dendritic and 'clover-leaf' morphologies should be investigated.

In purely macroscopic solidification models that take fluid flow in the mushy zone into account, the specific surface area that appears in the Kozeny-Carman relation is commonly assumed to be a constant. Due to the problems with assessing the morphology development during solidification, as discussed in Article 3, this assumption has not been validated. Because the existing models for equiaxed growth indicate that the assumption of a constant specific surface area is in fact *not* valid, this assumption is likely to induce a large error in the permeability even though the Kozeny-Carman relation by itself is a good model. The same argument applies to the more recent permeability model used in Article 1: The model seems to represent a very accurate description of the permeability as a function of a set of morphology parameters. However, because we lack a validated model for the development of the parameters at which the permeability depend, we can not expect to have a very accurate prediction of the permeability during solidification. For the samples in Article 3, the comparison between measured and modelled morphologies indicates that the permeability is overestimated by a factor of 10. Thus, presently, the accuracy of the permeability used in solidification models is limited by the assumptions concerning the morphology development rather than the assumptions concerning the relation between the morphology and the permeability.